Surface layer formation in polymer melts and in solutions

Dissertation

zur Erlangung des Grades „Doktor der Naturwissenschaften"
am
Fachbereich Chemie und Pharmazie der Johannes Gutenberg-Universität
Mainz

vorgelegt von
Rüdiger Stark
geboren in Marburg/Lahn
Mainz, Januar 2007

Contents

List of Figures

List of Tables

Abstract

In this work the surface layer formation in polymer melts and in polymer solutions have been investigated with the atomic force microscope (AFM). In polymer melts, the formation of an immobile surface layer results in a steric repulsion, which can be measured by the AFM. From former work it is know, that polydimethyl siloxane (PDMS) forms a stable surface layer for molecular weights above 12 kDa. In the present thesis, polyisoprene (PI) was investigated apart from PDMS, by a) measuring the steric surface interactions and b) measuring the surface slip in hydrodynamic experiments. If a polymer flows over a surface, the flow velocity at the surface is larger then zero. If case of a surface layer formation the flow plane changes to the top of the adsorbed layer and the surface slip is reduced to zero. By measuring the surface slip in hydrodynamic experiments, it is therefore possible to determine the presence of a stable surface layer.

The results show no stable repulsion for PI and only a small decrease of the surface slip. This indicates that PI does not form a stable surface layer, but is only adsorbed weakly to the surface.

Furthermore for 8 kDa PDMS the timescale of the formation of a surface layer was investigated by changing the maximal force the tip applied to the surface. With a repulsive force present, applying a higher force than 15 nN resulted in a destruction of the surface layer, indicated by attractive forces. Reducing the applied force below 15 nN then resulted in an increase of the repulsion to the former state during one minute, thus indicating that a surface layer can be formed within one minute even under the influence of continuous measurements.

As a next step, mixtures of two PDMS homopolymers with different chain lengths have been investigated. The aim was to verify theoretical predictions

that shorter chains should predominate at the surface due to their smaller loss in conformational entropy. The measurements where done in dependence of the volume fractions of short and long chain PMDS. The results confirmed the short chain dominance for all mixtures with less then 90 vol.% long chain PDMS.

Surface layer formation in solution was investigated for superplasticizers which are industrially used as an additive to cement. They change the surface interaction between the cement grains from attractive to repulsive and the freshly mixed cement paste therefore becomes liquid. The aim in this part of the thesis was, to investigate cement particle interactions in a close to real environment. Therefore calcium silicate hydrate phases have been precipitated onto an AFM tip and onto a calcite crystal and the interaction between these surfaces have been measured with and without addition of superplasticizers. The measurements confirmed the change from attraction to repulsion upon addition of superplasticizers. The repulsive steric interaction increased with the length of the sidechain of the superplasticizer, and the dependence of the range of the steric interactions on the sidechain length indicated that the sidechains are in a coiled conformation.

1 Introduction

Polymers at solid-liquid interfaces have been studied to a great extent due to their relevance in colloidal systems, fabrication of composite materials, paints, concrete admixtures, and for fundamental reasons, such as investigating the structures of adsorbed layers, their stability and their adsorption kinetics. Adhesive polymer layers are used for lubrication, coatings, and – generally spoken – to modify the surface forces at the interface.
The probably most common use of a surface polymer layer is the stabilization of colloids in liquids. From the entangled polymer layer around the colloid particles a repulsive steric force arises, which can e.g. stabilize a paint so it stays fluid over a long period of time, or make a cement paste fluid enough to form a horizontal and even surface when poured on the ground. Under certain circumstances, the polymers can also bridge the distance between two particles and bind to both of them. This leads to flocculation in contrast to the steric repulsion mentioned before.
The research of the last 60 years has been mostly focused on the formation of polymer layers from an aqueous and solvent environment [1], while the understanding of the forces occurring in polymer melts is still rudimentary. Therefore the interaction between two solid surfaces across a polymer melt has been studied theoretically [2–6], in simulations [7, 8] and experimentally. Experimental techniques to measure surface forces in a polymer melt are the surface force apparatus (SFA), with which PDMS [9–12], perflourinated polyether (PFPE) [13–15], polybutadiene (PB) [16, 17], polyisoprene (PI) [18] and poly(phenylmethylsiloxane) (PPMS) [9, 19–21] have been studied, and the atomic force microscope (AFM) where mostly PDMS, PEMS and PI have been studied [22–26].
In recent experiments, PDMS of different molecular weight was been in-

vestigated with the AFM [24–26], with the result that polymers above the molecular entanglement weight of M_e = 12 kDa [27] showed only repulsive forces. This indicates the presence of a immobilized surface layer, which was in agreement with earlier results from SFA experiments [28–30]. In contrast to the SFA, the AFM measurements for PDMS below the entanglement molecular weight showed attractive forces. Apparently some minimum degree of entanglement is required to form a stable surface layer.

Differences between these two techniques are the interaction area, and the sample surfaces. For the SFA, the interaction is measured between two crossed mica cylinders, which have radii in the range of one centimeter which results in large interaction areas compared to the AFM.

The AFM has the advantage that it is not restricted to mica surfaces. Since the interaction area is much smaller, hydrodynamic forces can be neglected and the measurements can be seen as quasi-static.

The relevant processes in a polymer melt which have to be considered for SFA and AFM measurements are: Relaxation of the individual chains, which is much faster than 1 s and which is achieved both in SFA and AFM experiments, and the flow of the polymer into and out of the closing gap between two surfaces to establish equilibrium with the surrounding polymer melt. For the SFA, the flow is usually too slow to equilibrate the gap with the surrounding [31,32].

Another surface property where the formation of a surface layer becomes important is the surface slip. For a Newtonian* fluid it is usually assumed that the velocity of the liquid at the surface is zero during shearing, which is called the non-slip boundary condition. This behavior, is different for a polymer (a non-Newtonian fluid), where the velocity at the surface is larger than zero due to an immobile polymer layer on the surface. By measuring hydrodynamics in a polymer melt, it is therefore possible to gather information on the formation of an immobile surface layer, since the layer changes the appearance an the amount of surface slip. In the AFM this can be achieved by the

*__Newtonian fluid:__ A fluid whose stress at each point is linearly proportional to its strain rate at that point; the proportionality factor is the viscosity coefficient. The concept was first deduced by Isaac Newton and is directly analogous to Hooke's law for a solid. All gases are newtonian, as are most common liquids such as water, hydrocarbons, and oils.

colloidal probe technique [33,34]: A microsphere with a radius of 5 - 10 µm is attached on a cantilever, and driven towards a flat surface with speeds up to 100 µm/s. Under such conditions, the hydrodynamic force dominates, and the measured interactions can be fitted with a model to determine wether a surface layer is present or not.
The aim of this work is to give new insights into the molecular weight dependent formation of immobile surface layers in polymer melts. Starting with PDMS, and working in quasi-static conditions, and then extending the focus to PI and hydrodynamic measurements. Based on these results, also mixtures of homopolymers have been investigated to get information about the competitive adsorption of chemically identical polymers with different chain lengths. This has been investigated before by scattering methods [35], with the result that shorter polymer chains enrich at the surface due to their smaller loss in conformational entropy. The disadvantage of such scattering experiments is, that the polymer needs to be deuterium labeled to achieve a contrast. Unfortunately, the interaction energy of protonated and deuterated polymers with the surface are different, and the labeling therefore influences the adsorption behavior. With the AFM, it is possible to distinguish between PDMS below and above the molecular entanglement weight without labeling.
As mentioned in the beginning, though, polymer surface layers also play a significant role in industry products, especially in aqueous environments. Therefore the aim of this work becomes twofold: First the fundamental research in polymer melts, and second the application of polymer surface layers in an industrial product. One of such products are superplasticizers which are used in concrete paste to enhance the flow by inhibiting the aggregation of the cement particles during the first stage of the cement hardening. Although superplasticizers provide a similar steric repulsion to the particles, their structure and adsorption mechanism is quite different. Due to ion-ion correlations, they attach to the surface of the cement particles with polymer chains protruding into the surrounding space, thus generating the steric repulsion. The degree of steric interaction can be controlled with the length of the sidechains.

The aim of this part of the work was to establish a working environment for measuring cement particle interaction under the influence of different ion concentrations and superplasticizers. After establishing an experimental setup and verifying the CSH crystal growth by imaging the lattice dimensions on the surface specific, effects of superplaticizers on the CSH surface were studied.

The thesis is divided into four main parts:
In chapter one, the the theory of polymer adsorption, surface forces, hydrodynamic forces, and the AFM are presented. A brief introduction into the forces important in cement cohesion and its hardening process over time is given.
In chapter two, the used materials and methods are described, including the specific setup for the AFM experiments, the differences between quasi-static and hydrodynamic measurements, and the details of preparing CSH surfaces for AFM measurements.
In chapter three, the results are described in detail and interpretations are put in relation with the introduced models and with the theory.
In chapter four, the main results of the thesis are summarized and conclusions are drawn.

2 Fundamentals

2.1 Polymer adsorption

The adsorption of polymers on surfaces is a long known technique to modify the surface properties, e.g. the wettability, steric repulsion, and friction forces, or introducing functionalized groups to the surface. Despite its importance, polymer adsorption is still not fully understood, and therefore focus of extended research. The reason for the complexity of the subject are the many different factors that play a role in the adsorption process. Polymers can be either adsorbed chemically by forming covalent or hydrogen bonds to the surface, or physically, by van der Waals forces. The chain length of the polymer, as well as differently functionalized chain ends, influences the adsorbed layer by changing entropy and free enthalpy of the chain in solution and at the surface. In solution, also solvent-polymer interactions influence the adsorption process.
This work covers three different systems with different driving forces for the formation of an adsorbed polymer layer: (i) The adsorption from a pure polymer melt, (ii) the competitive adsorption from mixtures of a homopolymer with two different chain lengths, and (iii) the adsorption of a "bottle-brush" polymer (a backbone with sidechains) from solution.
To discuss the properties of these systems in detail, this chapter introduces parameters such as adsorbed amount, adsorption entropy, Kuhn length and radius of gyration, and discusses layer structures like brush-like layers and solidification.

2.1.1 The polymer chain

An *ideal polymer chain* can be described as a chain with N freely jointed segments (monomers) with the length a, or a number of bonds n with a length l, which follow a random walk with the jump vectors $\vec{a}_i$ (or $\vec{l}_i$) and the end-to-end vector $\vec{r}$. If the jump vectors are summed up, this leads to the average of:

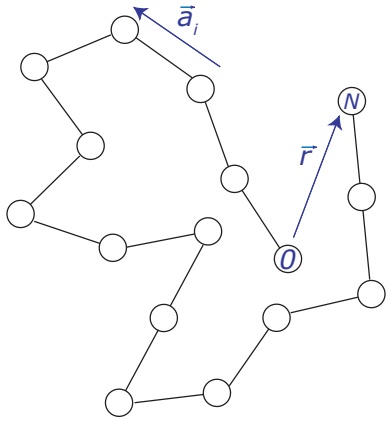

Fig. 2.1: Schematic picture of a polymer chain. The end-to-end vector $\vec{r}$ is the sum of all jump vectors of the monomers $\vec{a}_i$. The contour length r_{max} is the sum of all distances a_i.

$$\left\langle r^2 \right\rangle = Na^2 = nl^2 \tag{2.1}$$

The average of the square of the end-to-end vectors gives information about the conformation of the chain. The maximum end-to-end distance is equal to the contour length, smaller distances indicate a coiled conformation.

This simple model neglects the fact that the bond angles in the chain are restricted and that short distance correlations exist, especially between neighboring segments. Taking these interactions into account, it can be shown that the basic random walk character of the chains does not change. The calculations then result in a prefactor, also called Flory's characteristic ratio C_∞, which depends on the restriction of the bond angles and the steric hindrance in the chain, and has values from 5-9 for most polymers. Alternatively the prefactor can be mutiplied by the monomer size to an "effective step size" ($b = C_\infty \cdot a^2$). The length b is called the Kuhn length.

$$\left\langle r^2 \right\rangle = Nb^2 = C_\infty Na^2 = C_\infty nl^2 \tag{2.2}$$

The contour length is now simply $r_{max} = Nb$.

By going from an ideal chain to a *real polymer chain* in solution, the effect of the solvent has to be included in the equations. The solvent causes the polymer coil to swell or contract depending on the solvent-polymer interactions. If they are stronger than polymer-polymer interactions, solvent is incorporated into the coil and it swells (*good solvent*). If the polymer-polymer interactions are stronger, the coil contracts (*bad solvent*). If both interactions are similar the polymer coils display an ideal random walk without solvent influences, this is called θ-conditions.
A swollen polymer coil includes additional volume which is called "excluded volume". This results in an exponent ν for the number of monomers which is in the order of $1/2$ if the coil is neither stretched nor contracted (θ-conditions, $r = N_K^{0.5} b$), increases to $3/5$ for good solvents, and drops below $1/2$ for bad solvents.
A polymer is not only defined by its end-to-end distance, but also by its radius of gyration. This is a much more descriptive property for polymers in a coil conformation and highly branched polymers, since it represents the measurable radius of one polymer coil and not a statistic length inside the polymer matrix. The radius of gyration is defined as the average square distance between monomers and the polymers center of mass in a given conformation. It can be calculated as

$$R_g^2 = \frac{\langle r^2 \rangle}{6} = \frac{N_K^{\nu}}{6} b^2 \tag{2.3}$$

Again for the radius of gyration, the solvent interactions can cause the polymer coil to swell or to contract, changing thus the exponent ν.

2.1.2 The adsorbed layer

Concentration

Adsorption is an increase in concentration in the interfacial region. If the adsorption involves formations of chemical bonds between the polymer and the surface the adsorption is denoted *chemisorption* and is usually more stable. If only physical forces play a role, the adsorption is denoted *physisorption*.

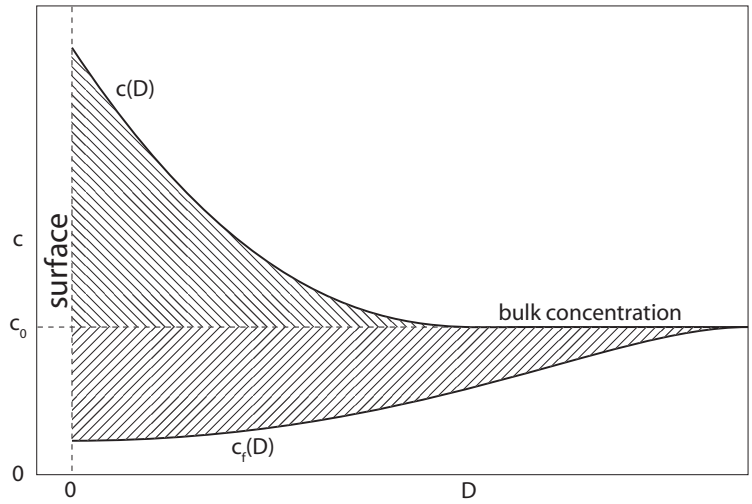

Fig. 2.2: Concentration profile of a polymer layer vs. distance. If the polymer chains is divided into segments, $c(D)$ is the overall segment concentration, $c_f(D)$ is the concentration of segments of non-adsorbed chains.

Such adsorbed layers can be described by a concentration profile with the concentration $c(D)$ as function of the distance D from the interface. The concentration gradually drops to the value of the average bulk concentration at a distance of approximately 1 - 2 times the radius of gyration, which is in the order of a few nanometers. An important parameter that can be deduced from the polymer concentration is the adsorbed amount Γ. If adsorption from a very diluted polymer solution is considered, the adsorbed amount is simply the area under $c(D)$.

For a polymer melt, the polymer segment concentration does not change significantly between surface and bulk. Therefore the concentration of non-adsorbed chains vs. the distance is considered ($c_f(D)$) and the adsorbed amount is the area between the bulk concentration and $c_f(D)$. For an adsorbed layer in a polymer melt, this profile increases from zero at the interface to the bulk concentration, so in a general case, the adsorbed amount is the area between $c(D)$ and $c_f(D)$ (Fig. 2.2) [1].

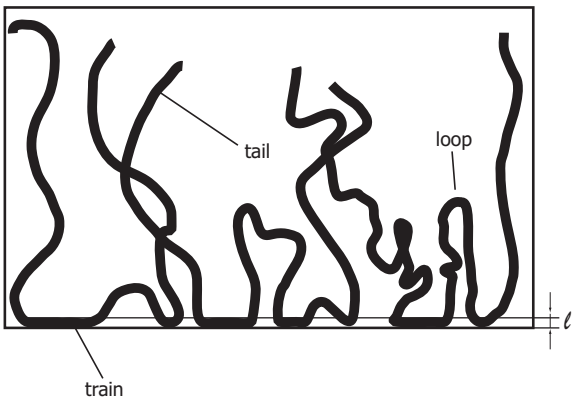

Fig. 2.3: Structure of a polymer layer adsorbed to a surface. Train, loops and tails are indicated. ℓ is the thickness of the chain.

Structure

A polymer chain is usually attached to the surface by a number of segments along its length. The structure consists of trains, tails and loops (Fig. 2.3). Trains are the parts of the polymer which have all their segments in direct contact with the surface, loops have no contacts with the surface and are in between two trains, and tails are the non-adsorbed chain ends. The layer on the surface can also be seen as a mesh of polymer chains. For a polymer volume fraction φ and a monomer size b the mesh-size is given as $\xi = b\varphi^{-3/4}$. The layer can be described as a self-similar grid (Fig. 2.4) for which at any distance D from the wall, the local mesh size is equal to D. The volume fraction $\varphi(D) = \frac{D}{b}^{-4/3}$ obeys a power law.

Adsorption thermodynamics

When a polymer adsorbs on a surface, it gains energy from the binding to the surface, and loses entropy from the restriction in conformation due to the surface. The conformational entropy loss is only dependent of the length of the polymer chain. In statistic thermodynamics the entropy is defined as

$$S(N,\vec{r}) = k_B\Omega(N,\vec{r}) \tag{2.4}$$

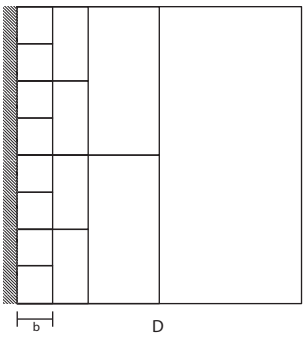

Fig. 2.4: Self-similar grid of a polymer layer. At any distance D from the wall the local mesh size is equal to D

$\Omega(N, \vec{r})$ is the number of conformations of an ideal chain. Since a longer chain has a greater number of conformations, its entropy loss at the surface is larger. Without considering any other interactions, short chains are favored over long chains to be adsorbed onto the surface. This is e.g. the case for a binary mixture of two identical polymers with different chain lengths in a melt.
The entropic contribution is usually small compared to the interaction energies between polymer, solvent and interface. Therefore in a binary mixture of *chemically different* polymers, only the component with the highest surface-polymer interaction adsorbs. Entropy becomes important only for identical polymers of different chain lengths in absence of a solvent. Even for a mixture of polymer melts of e.g. PS with deuterated-PS, the chain length differences must be large (factor 10) in order to overcome the difference in interaction energy between deuterated to non-deuterated PS [35].

Adsorption from solution

The adsorption from a diluted polymer solution differs from the situation in a polymer melt by the additional influence of the solvent, which is now competing with the polymer for the surface. Additional solvent surface and solvent polymer interactions have to be considered. The surface interactions are still the driving force for chemically different polymers, but now the mixing

entropy favors long polymer chains at the interface for homopolymer mixtures. Fleer et al. [1] give the mixing entropy from the Flory-Huggins theory as

$$(S - S^*) / k_B = -n \left\{ \varphi_1 \ln \varphi_1 + \frac{\varphi_2}{N} \ln \varphi_2 \right\} \tag{2.5}$$

The solution is described as a lattice containing n sites, of which $n\varphi_1$ are occupied by solvent and $n\varphi_2$ are occupied by polymer segments. S^* is the reference state of pure unmixed components, N is the number of segments per chain. For longer chains, N increases, and the entropy decreases. Therefore the entropy loss of longer chains adsorbing on the surface is smaller.

Polymer brushes

Polymer chains can also be terminally attached by directly grafting them on the surface, or by using a copolymer with a backbone attached to the surface and sidechains protruding into the solution. In the case of a high grafting density (large amount of attached chains per area), they display a stretched conformation with a high segment density at the surface, and the concentration profile is constant for the distance of the chain length. This is called a polymer brush. For a fully stretched conformation, the chain dimensions vary linearly with N. Only for smaller grafting densities, a coil conformation is reached and the exponent ν decrease to $3/5$.

Solidification

If a high pressure (from e.g. an AFM tip) acts upon the adsorbed layer, the polymer might undergo a phase transition and become solid. Since a thin polymer layer behaves differently from the bulk, it is difficult to estimate such solidifications. The possibility of solidification of a polymer melt in an AFM experiment will be discussed in detail in section 2.8.

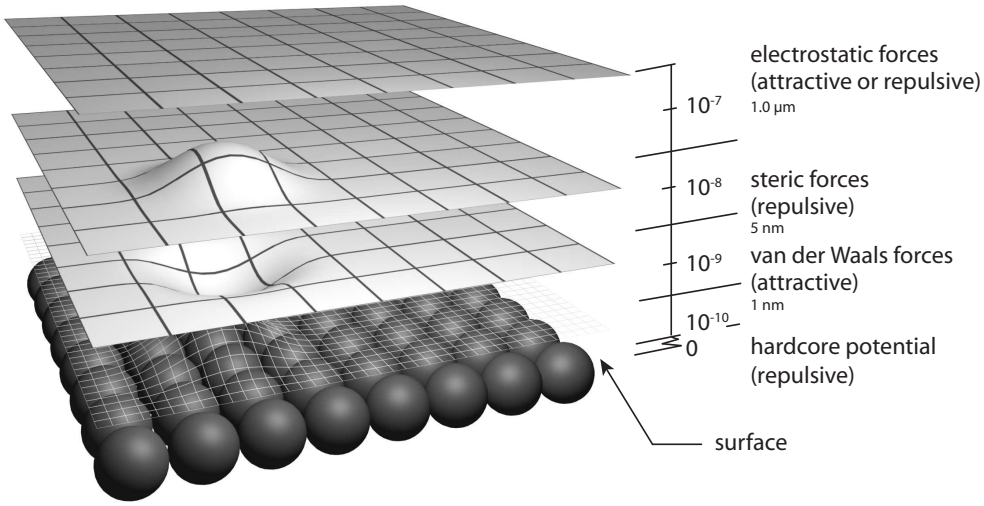

Fig. 2.5: Overview of the surface fores present in AFM measurements

2.2 Surface forces

Surface forces act between the surfaces of all solids. They control e.g. aggregation and adhesion and can therefore be responsible for even macroscopic properties. Fig. 2.5 provides an overview of the surface forces measured with the AFM in this work, in dependence of the separation between two surfaces.

2.2.1 The Hardcore potential

The hardcore potential (Pauli repulsion), arises from the fact that two atoms cannot occupy the same space. As soon as two atomic orbitals start to overlap, the repulsion between them drastically increases. This repulsion is very short ranged and decays with D^{-12}.

2.2.2 The an der Waals forces

Van der Walls forces are forces between two dipoles (permanent or induced). The most common example of a dipole is the water molecule. The oxygen is more negatively charged than the hydrogen and the molecule therefore align

preferentially to an electric field caused by e.g. an external single charge. The interaction of two water molecules can then be described as the interaction of two dipoles. They both influence their orientation and display continuous thermal fluctuations. The dipole-dipole interaction for freely rotating dipoles with their dipole moments (μ_1 and μ_2) is given by:

$$W = -\frac{C_{Keesom}}{D^6} = -\frac{\mu_1^2 \cdot \mu_2^2}{3(4\pi\varepsilon_0)^2 k_B T D^6} \tag{2.6}$$

The force between to permanent dipoles is called *Keesom force* and depends on the thermal energy ($k_B T$). These dipole dipole interaction decrease with the distance with D^{-6}.

Dipoles are not always permanent, but can also be induced by an external field. A measure of how easily a dipole can be induced is the polarizability α. The force between a permanent dipole and an induced dipole is called *Debye force*:

$$W = -\frac{C_{Debye}}{D^6} = -\frac{\mu^2 \alpha}{(4\pi\varepsilon_0)^2 D^6} \tag{2.7}$$

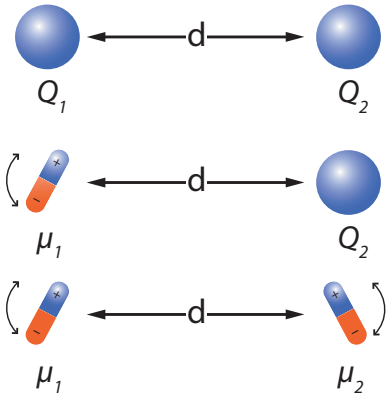

Fig. 2.6: Coulomb interactions between monopoles and dipoles. The dipoles fluctuate thermally.

For non-polar molecules, we would not expect any interaction from classical electro-dynamics. However, since all gases condense at low temperatures, there must be an attractive force [36]. This so called dispersion or *London forces* originate from the fluctuation of the charge distribution from protons and electrons in atoms. The polarity changes very fast, but this nevertheless results in a dipole. To calculate such forces, quantum mechanics are used, but the result is quite similar to the one obtained before, with $h\nu_1$ and $h\nu_2$ as ionization energies.

$$W = -\frac{C_{London}}{D^6} = -\frac{3}{2} \cdot \frac{\alpha_1 \alpha_2}{(4\pi\varepsilon_0)^2 \cdot D^6} \cdot \frac{h\nu_1 \nu_2}{(\nu_1 + \nu_2)} \tag{2.8}$$

Keesom, Debye and London forces sum up to the total van der Waals force and decrease with D^{-6}. Since the change of the dipole moment requires some time (10^{15} Hz) it may happen that the dipole moment changes too fast for the electric field to cover the distance to induce the dipole. This effect is called retardation and is relevant for distances larger than 10 nm. The interaction decreases more steeply (D^{-7}).

2.2.3 The Lifshitz theory

To calculate the magnitude of the interactions between macroscopic bodies, e.g. a point charge and a infinitely extended plane, it is necessary to integrate over the molecular density of the entire plane. Starting from the potential between two molecules ($W = -C/D^6$), the molar density ρ_B is integrated over the entire volume of the solid. By assuming a constant density of the molecules in the solid, we get the van der Waals energy between a molecule A and an infinitely extended body with a planar surface made of molecules B:

$$W_{Mol/Plane} = -\frac{\pi \rho_B C_{AB}}{6D^3} \tag{2.9}$$

Integration over all molecules in the solid A leads to the van der Waals energy between to infinitely extended solids with a re separated by a parallel gap with the thickness D. The energy is given per unit area:

$$w = \frac{W}{A} = -\frac{\pi \rho_A \rho_B C_{AB}}{12D^2} \tag{2.10}$$

With w the area dependent potential energy and ρ the molecular densities. To get the force per area, the negative derivative of w versus the distance is calculated.

$$f = -\frac{A_H}{6\pi D^3} \tag{2.11}$$

with A_H as the Hamaker constant defined as:

$$A_H = \pi^2 C_{AB} \rho_A \rho_B \tag{2.12}$$

To calculate the van der Waals forces between two surfaces, Lifshitz introduced a way to determine the Hamaker constant by integration over the static and frequency dependent dielectric permittivity of the materials [36,37].

$$\begin{aligned} A_{AB} &\approx \frac{3}{4}k_B T \left(\frac{\varepsilon_1 - \varepsilon_3}{\varepsilon_1 + \varepsilon_3}\right)\left(\frac{\varepsilon_2 - \varepsilon_3}{\varepsilon_2 + \varepsilon_3}\right) \\ &+ \frac{3h}{4\pi}\int_{\nu_1}^{\infty}\left(\frac{\varepsilon_1(i\nu) - \varepsilon_3(i\nu)}{\varepsilon_1(i\nu) + \varepsilon_3(i\nu)}\right)\left(\frac{\varepsilon_2(i\nu) - \varepsilon_3(i\nu)}{\varepsilon_2(i\nu) + \varepsilon_3(i\nu)}\right)\mathrm{d}\nu \end{aligned} \tag{2.13}$$

Lifshitz neglects the atomic structure of the materials and treats the solids as continuous media with certain optical properties. ε are the static dielectric permittivities and $\varepsilon(i\nu)$ are the dielectric permittivities at the imaginary frequency $i\nu$, and $\nu_1 = 2\pi k_B T/h = 3.9 \cdot 10^{13}$ Hz at 25°C. $\varepsilon(i\nu)$ can be written as

$$\varepsilon(i\nu) = 1 + \frac{n^2 + 1}{1 + \nu^2/\nu_e^2} \tag{2.14}$$

with n as the refractive index and ν_e as the main electronic absorption frequency in the ultraviolett, which is typically $3 \cdot 10^{15}$ Hz.

2.2.4 Steric forces

Steric forces are always repulsive and arise from a steric hindrance due to an adsorbed immobile surface layer, or a polymer brush. They are usually much stronger than van der Waals forces and depend on the thickness of the surface layer and its structure (brush or coil conformation).
Steric forces are the only ones in this work which can be manipulated mechanically. They might differ locally on the measured sample, or change due to increased pressure on the surface, or decrease by wear of the sample with time.

2.3 The hydrodynamic force

2.3.1 The Navier-Stokes equation

To calculate the hydrodynamic forces acting on a sphere in a liquid, the first step is to calculate the flow of a viscous Newtonian liquid in a pipe or over a surface using the Navier-Stokes equation.
Given that the viscosity of the liquid does not change when it is sheared, the equation describes an infinitesimal amount of the liquid with the volume $V = dx \cdot dx \cdot dz$, the flow velocity dv, and the mass dm. The flow of the liquid can be described by Newton's equation of motion ($F = m \cdot \frac{dv}{dt}$) where several forces have to be taken into account [36].
First, gradients in the shear force cause a viscous force according to $\eta \nabla^2 \vec{v} \cdot dV$. With η as the viscosity and $\vec{v}$ the flow vector. Second, a possible pressure (P) gradient results in the force $-(\nabla P) \cdot dV$. And third, an external electric field causes an electrostatic force on the ions in solution $\rho_e \vec{E} \cdot dV$. Where E is the electric field strength and ρ_e the charge density caused by the dissolved ions. combining the contributions leads to

$$\left(\eta \nabla^2 \vec{v} - \nabla P + \rho_e \vec{E}\right) dV = dm \cdot \frac{d\vec{v}}{dt} \tag{2.15}$$

If the fluid velocity is constant the equation reduces to

$$\eta \nabla^2 \vec{v} - \nabla P + \rho_e \vec{E} = 0 \tag{2.16}$$

For incompressible Newtonian liquids, the equation of continuity applies. The first derivative of the velocity in all directions is constant:

$$\nabla \vec{v} = \frac{\partial v_x}{\partial x} + \frac{\partial v_y}{\partial y} + \frac{\partial v_z}{\partial z} = 0 \tag{2.17}$$

Using these basic equations, it is possible to derive the hydrodynamic force of a sphere approaching a surface. Detailed discussions can be found in the literature [38, 39].
There are however two assumptions to be made. To ensure creeping flow

(inertia effects can be ignored in comparison to the viscous resistance), the sphere approaching the surface must be sufficiently small to result in a Reynolds number of less than $\ll 1$ ($Re = \rho v R/\eta$), and the velocity of the liquid at the surface has to be zero (non-slip boundary condition). Considering the symmetry of the approach, this leads to a hydrodynamic force on the approaching sphere in dependence of the distance (D) and velocity.

$$F_h = -\frac{6\pi\eta R^2}{D} \cdot \frac{dD}{dt} \tag{2.18}$$

Here dD/dt is the approaching velocity of the sphere. The force is directed opposite to the velocity.

2.3.2 The hydrodynamic boundary condition

To introduce surface slip, it is easiest to look at a system where a liquid flows over a molecularly smooth surface, being sheared between to parallel plates. The velocity of the liquid continuously decreases towards the wall, which ideally results in a velocity of zero at the wall. This approximation is valid for all Newtonian liquids.
Different results have been predicted for non-Newtonian liquids up to 50 years ago in dependence of the wetting behavior of the surface [40–42] and were confirmed in experiments with Polyvinylalcohol [43], PDMS [11,44–46], perflourinated polyether [14], PPMS [9]), PE [47], PB [17,48], PS [49], LDPE, EVA (polyethylvinylactetate) [50], and Boger fluids [51]. Under specific conditions, all these liquids show a velocity larger than zero at the interface - the liquid slips over the surface. The slip can be characterized from the velocity profile by the distance behind the wall at which the liquid velocity extrapolates to zero. The slip velocity is than given by $v_s = b \cdot dv_x/dy$ where v_s is the slip velocity on the surface, dv_x/dy is the local shear rate at the surface (x is the direction of the flow, z is directed normal to the surface), and b is the slip length (Fig. 2.7). This was first defined by Brochard [52]. Since that time, the appearance of surface slip has been discussed theoretically [40,42,52–57], in simulations [58–61] and experiments [9,11,14,17,43–48,50,51,62–74]. Experimental methods range from measuring enhanced drainage velocities [72],

measuring the capillary flow [43, 47, 50], evanescent waves [46, 69], dielectric relaxation spectroscopy [67], attenuated total reflectance fourier transform infrared spectroscopy [66], near field laser velocimetry [68], to the surface force apparatus (SFA) [11, 14, 17, 51, 73, 74] and the AFM [22, 62, 63, 71]. Noteworthy is the gained insight made by Pit [70], that slip occurs also in Newtonian liquids if the surface is hydrophobic or partially wetting [75, 76]. Further on, slip was seen on hydrophilic surfaces too [63, 71]. A complete overview can be found in the reviews [77, 78].

In some systems at a certain distance, a "glassy" or "solid-like" layer is found. In such cases, the shear plane shifts from the sample surface to the layer surface, and no slip is observed anymore.

To measure hydrodynamic forces with the AFM, instead of a microfabricated tip a spherical particle is used to measure the surface forces. If the approaching velocity of the sphere is high enough, the hydrodynamic force dominates over all other surface interactions. Important parameters in these experiments are the approaching speed, the particle radius, the viscosity of the medium and the surface slip.

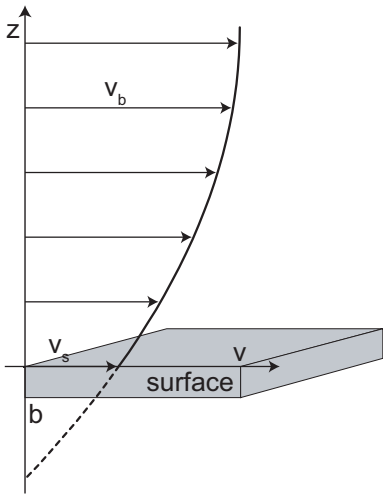

Fig. 2.7: View of the shear force near the surface with the velocity v_b. There is a finite velocity of v_s on the surface and the slip length b extrapolates into the surface.

The hydrodynamic force curves are simulated solving the equation of motion for a sphere moving towards - or retracting from - a plane in a fluid:

$$F_h + F_{vdW} + F_c + F_{drag} = m^* \cdot \frac{d^2D}{dt^2} \tag{2.19}$$

Here, D is the separation between sphere and flat surface, F_h is the hydrodynamic force on the sphere, F_{vdW} is the van der Waals attraction, F_c is the restoring force of the cantilever, F_{drag} is the hydrodynamic drag on the cantilever, and $m^* \frac{d^2D}{dt^2}$ takes a possible contribution of acceleration into account. Since our system is characterized by small Reynolds numbers ($Re \ll 1$) the acceleration term can be neglected and was not further considered. The dif-

ferent contributions are discussed in detail in Stark et al. [22] and result in two equations of motion, one for the approaching, one for the retracting part:

$$-\frac{6\pi\eta R^2}{D}\cdot\frac{dD}{dt}f^* - \frac{A_H R}{6D^2} + F_{drag} = \begin{cases} k_c(D - D_a + v_0 t), & \text{for } 0 < t \leq t_a \\ k_c(D - D_r - v_0 t), & \text{for } t_a < t \leq t_r \end{cases} \tag{2.20}$$

Here, D_a and D_r are the initial separations of the sphere and the plane, respectively for approach and retraction, while t_a and t_r are the approach and retraction times. k_c is the spring constant and v_0 the approaching velocity of the piezo. A_H is the Hamaker constant, which was estimated with $2 \cdot 10^{-21}$ J but turned out to barely influence the overall force. The initial conditions are

$$\begin{cases} D(t=0) = D_a, & \text{for } 0 < t \leq t_a \\ D(t=t_a) = D_r = 0, & \text{for } t_a < t \leq t_r \end{cases} \tag{2.21}$$

The hydrodynamic contribution in eq. 2.20 is given by

$$F_h = -\frac{6\pi\eta R^2}{D}\frac{dD}{dt}\cdot f^* \quad f^* = \frac{D}{3b}\left[\left(1+\frac{D}{6b}\right)\cdot\ln\left(1+\frac{6b}{D}\right)+1\right] \tag{2.22}$$

with the correction factor f^* introduced by Vinogradova [72]. Here, b is the slip length. It is a fitting parameter and is not measurable a priori, while all other parameters in eq. 2.22 can be independently determined from further measurements. The model assumes creeping flow (low Reynolds number), Newtonian fluids, and small distances ($D \ll R$). The differential eq. 2.20 cannot be solved analytically. A numerical solution was implemented in Maple V (Waterloo Maple Inc., Ontario, Canada).

2.4 The Hertz model

We look at the scheme in fig. 2.8 where we have a polymer layer on the surface, with the AFM tip applying a high pressure and thus indenting the layer. To estimate the layer stiffness and the indentation δ of the layer for the AFM tip or a glass sphere, the Hertz model [79] allows to calculate the

indentation in dependence of the force applied. The model describes very generally two spheres pressed together. The spheres are defined by their radii R, Young's moduli E and Poisson's ratios ν. The two spheres are pressed together by a force F. No further surface forces (e.g. van der Waals forces) are considered. The contact area is circular with a radius of a. If the pressure on the surface layer is integrated over the whole interaction area, the total force is given by

$$F = \frac{4E^*}{3R^*} \cdot a^3 \tag{2.23}$$

with R^* and E^* as the reduced radii and the reduced Young's modulus given as

$$R^* = \frac{R_1 \cdot R_2}{R_1 + R_2} \quad \text{and} \quad \frac{1}{E^*} = \frac{1-\nu_1^2}{E_1} + \frac{1-\nu_2^2}{E_2} \tag{2.24}$$

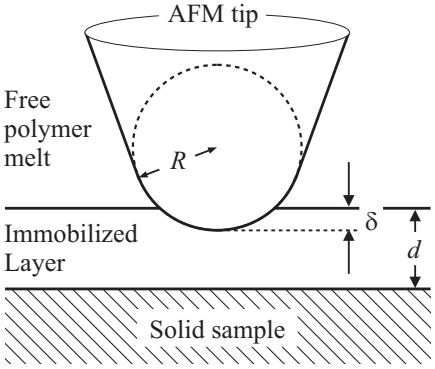

Fig. 2.8: Sketch of the Hertz model applied to the AFM setup with a layer and a hard sphere.

Since the contact radius is given as $a = \sqrt{\delta R^*}$, the force-versus-indentation relationship results in

$$F = \frac{4}{3} \cdot E^* \cdot \sqrt{R^* \delta^3} \tag{2.25}$$

In an AFM experiment, instead of two spheres approaching each other, a sphere approaches a plane surface. This results in $R^* = R_1$ and $\frac{1}{E^*} = 2 \cdot \frac{1-\nu_1^2}{E_1}$ for the reduced radius and Young's modulus.

In reality the immobilized layer has a finite thickness. A thin layer with a lower Young's modulus might exist and only due to the finite thickness it might appear hard. In this case our lower limit for Young's modulus might not be correct. To practically exclude such an effect we apply a complementary model, which is known as the solid foundation model or elastic foundation model [80]. The solids are modelled by a "matress" resting on a rigid

base being compressed by a rigid indenter. The shear between the adjacent elements of the foundation are ignored, thus a negligible Poisson ratio is assumed. Generally, the solid foundation model provides smaller values for the elastic modulus than the Hertz model. In the solid foundation model indentation and force are related by

$$F = \frac{\pi E R \delta^2}{D} \quad and \quad \delta = \sqrt{\frac{FD}{\pi E R}} \tag{2.26}$$

2.5 The Atomic Force Microscope (AFM)

2.5.1 General Setup

The atomic force microscope (AFM) was invented in 1986 by Binnig, Quate, and Gerber [81]. A sharp tip at the end of a cantilever is brought near a sample surface, so the surface interactions lead to a bending of the cantilever according to their strength and direction. The magnitude of the bending is measured by the deflection of a laser beam from the backside of the cantilever which hits a split photodiode (Fig. 2.9). From the voltage measured by the photodiode, it is possible to calculate the bending of the cantilever.
The sample surface can be moved horizontally and vertically to the tip by applying a voltage to a piezo crystal (scanner) on which the sample is mounted. To measure the surface forces, the scanner moves the sample periodically towards and away from the tip and the deflection is measured in dependence of the piezo position. If the spring constant of the cantilever is known, a force-distance curve (force curve) can be calculated.
A second measurement method of the AFM is the surface imaging. Here the scanner moves the surface laterally beneath the tip while minimizing the deflection. From the piezo positions, it is the possible to calculate the height profile of the sample surface. Both methods will be described in more detail in the following sections.

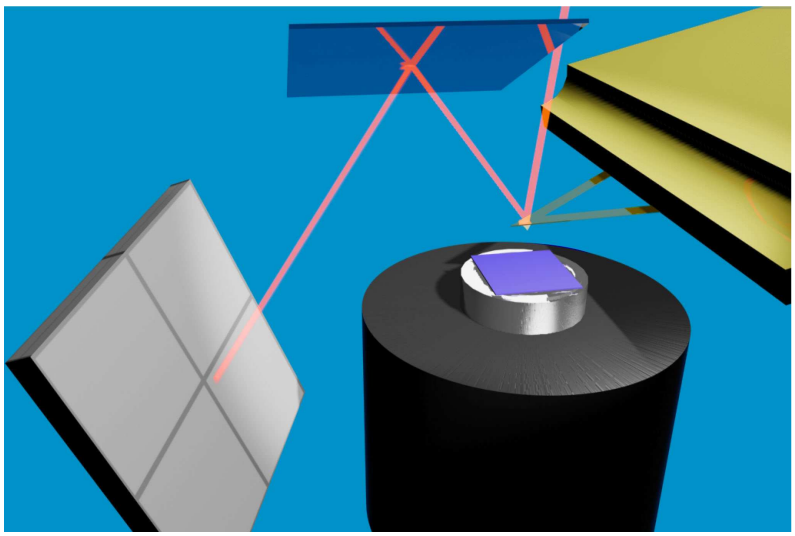

Fig. 2.9: Basic setup of an AFM. A laser hits the backside of the cantilever, which is bend up- or downwards depending on the surface interactions. The laser is reflected from the cantilever and a mirror onto a split photodiode, and induces a current in dependence of the intensity.

2.5.2 Force-distance-curves

Measuring force-distance-curves

As mentioned before, to measure force distance curves, the scanner moves periodically towards the surface and back again. This distance ("ramp size") can vary from 50 nm to 10 µm depending on the type of scanner used. The AFM measures the voltage* (U_{PSD}) in dependence of the piezo position (z_P), which is done for the *approach* and *retract* of the scanner.
From the measured voltage and the sensitivity of the photodiode (S_{PSD}), the deflection can be calculated: $d = U_{PSD} \cdot S_{PSD}$. The deflection d is than plotted vs the piezo position (*deflection curve*). This curve shows two linear parts: one where the tip is in contact with the surface, and one where there is no interaction between tip and surface (Fig. 2.11 left).
The deflection curve is then calibrated to a force-vs-distance curve (*force curve*). The linear part of the deflection curve where the tip is not in contact with the surface is used to define the zero force, and the constance compliance part is used to define zero distance. z_p is defined as zero, when the tip is in contact

*The laser induces a current in the photodiode which is then transferred into a voltage. Voltages can be more easily amplified and measured.

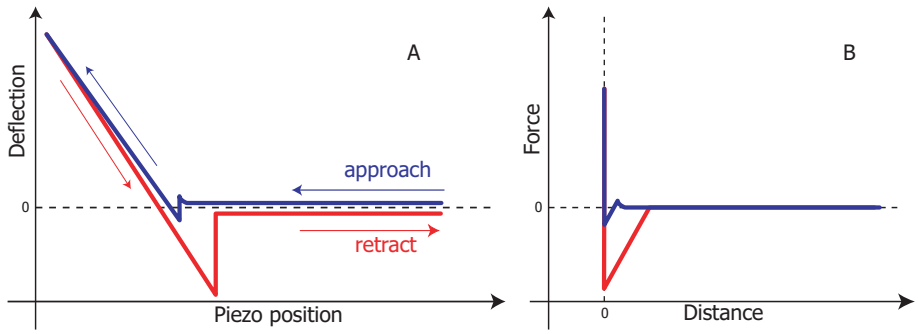

Fig. 2.11: Example of the calibration of a force-distance-curve. The two linear parts (zero force and constant compliance) are used to fix zero force and zero distance. a) shows the deflection-piezo position curve which is directly measured, b) shows the calibrated force curve.

with the surface and the cantilever is not bending.

The distance D between surface and tip (Fig. 2.10) can be calculated as $D = z_P - z_0 + d$. Where z_0 is the distance from the base of the cantilever to its tip.

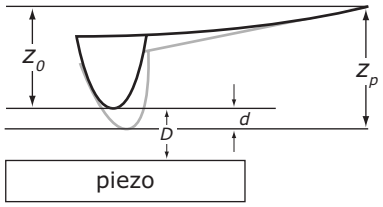

Fig. 2.10: Scheme of the bending of the cantilever. The distances are used for the calibration process.

The force F is calculated from the deflection by using Hook's law $F = k_c \cdot d$, using the spring constant of the cantilever k_c.

An example of a calibrated force curve is given in fig.2.11 (right).

The whole process of calibration is usually done automatically by a computer software, by defining the two linear parts of the deflection curve visually. The spring constant needs to be measured separately.

Interpretation of force-distance-curves

A force curve displays the forces acting on the tip in dependence of the tip-surface distance. Fig. 2.12 shows examples of different surface interactions for the approach. If the are no interactions at all, the cantilever is not deflected and the force is zero until the tip is in direct contact with the surface

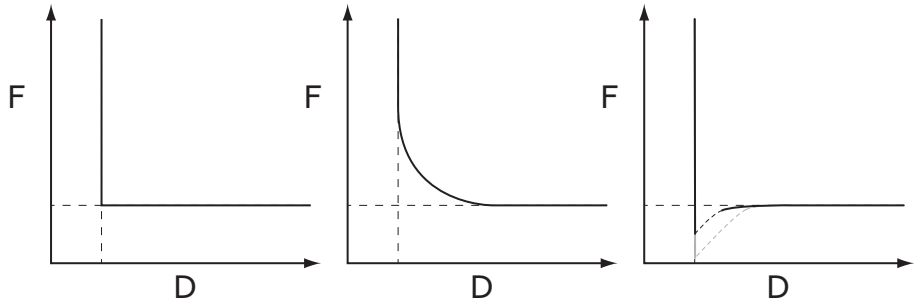

Fig. 2.12: Examples of force curves for no interaction (left), repulsive interaction (middle), and attractive interaction (right). Only approaching party are shown.

(left). If the surface interaction is repulsive, the cantilever is deflected away from the surface as soon as the tip is close enough to the surface. By approaching further, the interaction increases until the tip is in contact with the surface (middle). If the surface interaction is attractive, the cantilever is deflected towards the surface (right). With continuous approach, the interaction increases, until the restoring force of the cantilevers is overcome by the attraction - the tip snaps into contact (dashed line). For attractive interactions, the retraction diverges from the approach. The tip stays longer in contact with the surface and than snaps off (grey line).
Since in real systems, the surface interactions are a combination of several different forces (e.g. van der Waals forces and steric forces) with different ranges, force curves can also display repulsion for large distances, and attraction at close range. In such cases, the force curve needs to be fitted with an appropriate model to interpret the surface interactions correctly.
A general problem for the interpretation arises from the definition of zero distance. As mentioned earlier, zero distance is taken where the deflection increases linearly with the piezo position. So if a solid-like, not deformable layer is still on the surface, it is not possible to detect it [82] (for a detailed discussion see section 2.5.6).

2.5.3 Characteristics of cantilevers

Cantilevers are made of silicon nitride, silicon oxide or pure silicon. To ensure the reflection of the laser light, the backside can be coated with gold or alu-

minum. Important characteristics of a cantilever are the resonance frequency f_0 and the spring constant k_c.
From theory, the resonance frequency for a bar shaped cantilever is given by

$$f_0 = 0.164 \cdot \frac{d}{l^2} \cdot \sqrt{\frac{E}{\rho}} \tag{2.27}$$

Here h is the height and l the length of the cantilever. E is the Young's Modulus and ρ the density of the material.
For the spring constant, theory gives a value for bar shaped cantilevers with

$$k_c = \frac{Ewd^3}{4l^3}, \tag{2.28}$$

where w is the width of the cantilever.
However, cantilevers dimensions and material properties are not perfectly homogenous, therefore it is necessary to measure the spring constant for each cantilever individually. There are several methods to measure spring constants, the most popular is the use of a reference cantilever [83, 84] and measuring its thermal noise [85–87]. In the latter, the cantilever is modeled as an harmonic oscillator with the deflection Δd due to thermal fluctuations. If for an ideal spring the mean-square deflection $\left\langle \Delta d^2 \right\rangle$ is measured over all frequencies, the spring constant k_c can be calculated as

$$\frac{1}{2} k_c \left\langle \Delta d^2 \right\rangle = \frac{1}{2} k_B T \Rightarrow k_c = \frac{k_B T}{\langle \Delta d^2 \rangle} \tag{2.29}$$

However, the cantilevers used are not ideal springs due to several reasons. First, they display also higher vibration modes, which in sum all result in $\langle d^2 \rangle = k_B T / k_c$. Second, a correction factor has to be used to adjust for the individual cantilever shapes (bar shaped, V-shaped), and third, the added mass due to the tip at the end of the cantilever changes the vibration modes.
In practice, the spring constant is measured by recording a noise spectrum of the deflection and a force curve is taken to measure the sensitivity of the photodiode. The intensity of the noise spectrum is proportional to the inverse of the mean square deflection. This results in a Lorentzian function. The peak

at the resonance frequency from the first vibrational mode is then fitted with a lorentzian curve and integrated. The spring constant is given by

$$k_c = \beta^* \frac{k_B T}{\langle d_1^{*2}(L) \rangle} \tag{2.30}$$

With d^* as the effective measured deflection and β^* as a correction factor of 0.764 for V-Shaped and 0.965 for bar shaped cantilevers [36].

2.5.4 Imaging the surface

There are two commonly used methods of surface imaging with the AFM. One is the *tapping mode*, in which the cantilever oscillates at a specific frequency close to the surface. When the sample height increases, the oscillation is dampened and the piezo position is adjusted so the original specific frequency and amplitude is reached. The advantage is that the surface is only touched intermittently by the tip and it is therefore possible to image very soft samples, or surface features which are not firmly attached to the surface without destroying or moving them. A disadvantage is that in high viscosity fluids (e.g. polymer melts) the cantilever can not oscillate fast enough.
The second mode which was used throughout this work is the *contact mode* for which the tip touches the surface and the cantilever is slightly bend. If the sample height changes, the cantilever is bend upwards or loses contact, the piezo than adjusts the sample height again to minimalize the bending. The advantage here is that the scanning can be much faster than for tapping mode, and even in liquids and polymer melts, high resolutions can be achieved.
The resolution of the image is determined by the tip shape. The tip is generally assumed to have a spherical end with the radius R. By scanning across a surface, an image of the surface is produced as shown in fig. 2.13. There are two points of importance: First, indents in the surface will always appear smaller than in reality since the tip can not fully penetrate into them, second if the surface has spikes with smaller radius than the tip, the image will reflect the tip geometry, not the surface. However, if the tip geometry is known,

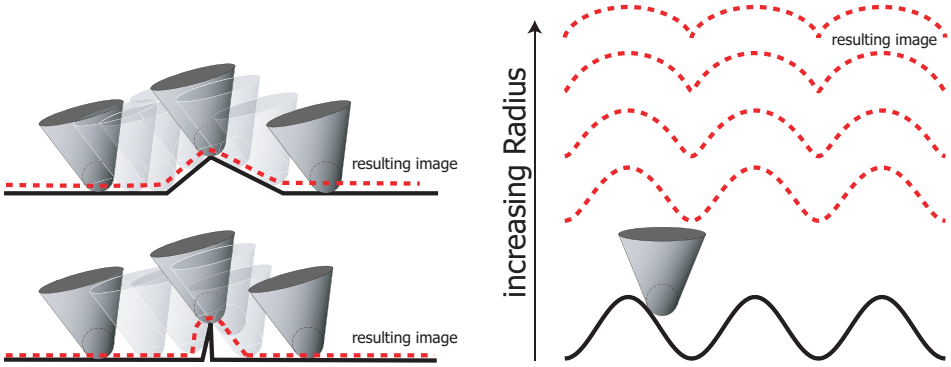

Fig. 2.13: Sketches how the sample surface is imaged by a cantilever tip. If the features on the surface are very "sharp", the image shows the tip instead of the surface. If the tip has a very large radius compared to the surface, the image shows smaller indents and larger exaltations.

there is the possibility to deconvolute image and the tip geometry using specific software (Scanning Probe Image Processor, SPIP, Image Metrology A/S, Hørsholm, Denmark).

While scanning the surface, it is not only possible to record the bending of the cantilever (x-direction), but also the tilt sideways to it (y-direction). By changing the scanning direction to 90°, the tip scans the surface sideways and the tilt of the cantilever is a measure for the friction between tip and surface. The friction mode can be used to distinguish between surfaces of the same height but different roughness (e.g. two different lipids forming a bilayer at the surface with different end-groups), or to measure lattice cells at the surface.

2.5.5 Measuring tip radii

Tip radii can be measured by imaging a grid with sharp spikes, or by taking scanning electron microscope (SEM) pictures and fitting circles into the tip shape. The advantage of taking SEM images is that an undistorted image of the tip is obtained, so defects of the tip can be seen directly. Such defects could be a blunt and non spherical tip shape due to very high pressure of the

tip on the surface, or the breaking of the functionalization (coatings) of the tip. Usual tip radii are in the order of 10 to 100 nm.

2.5.6 The definition of zero distance

The definition of zero distance in a force-distance experiment is an intrinsic problem of the AFM. As mentioned before, a force curve is calibrated by taking the two linear regimes where the tip is supposedly either in full contact with the surface, or is far away. If a solid layer covers the surface, or if a polymer layer is compressed, solidification of the layer might be possible. In such a case, we would be unable to detect the difference between the solid support and the hard polymer layer.

2.6 Adhesion in concrete and the effect of superplasticizers

2.6.1 Concrete

Portland cement clinker is the main component of the most common cements. It mainly consists of CaO (60%), SiO_2 (20%), Al_2O_3 and Fe_2O_3 (both together ca. 5%). By changing the ratio of these main components and by using various additives (e.g. sulfates, MgO, K_2O, MnO, or ZnO) the properties of the cement can be easily modified to produce, e.g. fast hardening or high stability cements.
In typical cement nomenclature, the main components are abbreviated as C (CaO), S (SiO_2), H (H_2O), A (Al_2O_3) and F (Fe_2O_3). In a cement clinker, they are already burned and grinded to alite (C_3S), belite (C_2S) and different aluminates. This burned clinker phases are then later mixed with water and harden to form cement (or concrete if additionally sand, gravel or steal is used). Since a clinker is made of so many different components, and all are reacting differently with water, it is very challenging to identify the processes of cement hardening and their individual time dependent contribution.

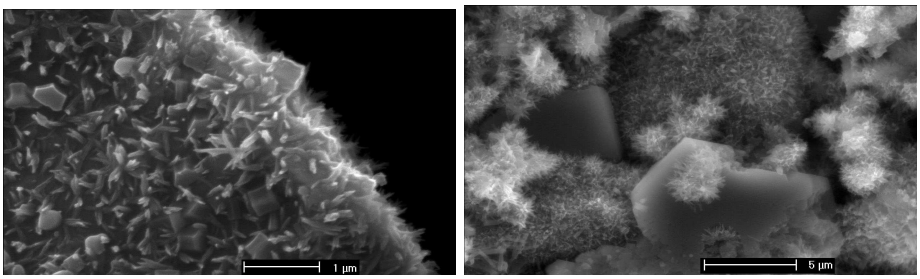

Fig. 2.15: REM images of the growth of the CSH crystals. At the beginning, the crystals show a honeycomb-like structure (left), after the first minutes, the CSH crystals grow only one dimensionally into needles (right).

Five important stages of the hardening process can be distinguished: First, the initial pre-induction period, which is exothermic and takes place in the first 15 minutes after mixing with water. Second, the dormant period (15 min - 3 h) where practically all reactions are stopped and the hardening process is discontinued. Third and fourth, the setting periods where the reaction rate respectively increases (3 - 8 h) and decreases again (8 h - 1 day), and where most of the final stability is reached. Fifth the diffusion period (1 day and longer), where no more thermal activity is present (Fig. 2.14) [88].

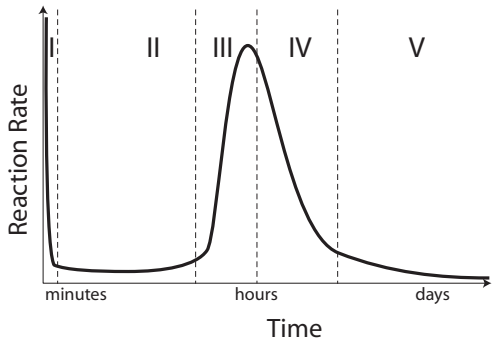

Fig. 2.14: The process of hardening is divided in five phases. It takes a month until all reactions are finished.

The important stages of the hardening process are the first four periods, where alite and belite play the most significant role by forming the so called CSH phases (calcium silicate hydrate phases) with an average composition of $C_3S_2H_4$. The CSH formation becomes visible after one hour and shows a honeycomb-like structure.

After the first hour, they start growing needles with about 50 nm diameter and hundreds of nanometers in length. The interlocking of these needles makes a significant contribution to the hardening of the cement.

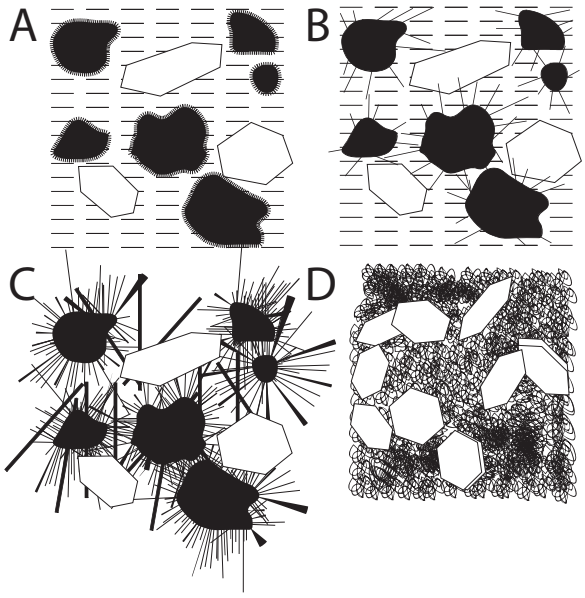

Fig. 2.16: Growth of the CSH crystals in a cement paste with time. First honeycomb like structures are build. Later, needles with a diameter of 50 nm and a length of several micrometers intercalate and form a solid structure.

The reactions taking place in a cement paste can be written as:

$$Ca_3SiO_5 + 2H_2O \quad \rightarrow \quad 3Ca^{2+} + 4OH^- + H_2SiO_4^{2-}$$

$$xCa^{2+} + yH_2SiO_4^{2-} + zOH^- \quad \rightarrow \quad C-S-H$$

At the first stage, the reaction with water increases the pH to 13 due to the dissociation of alite and belite. The calcium ion concentration is the main parameter controlling the hydration kinetics, stoichiometry and structure of the CSH phase [89,90].
During the first hour, the aggregation of the CSH particles is mainly due to the ion-ion correlations (Fig. 2.17). Later, during the formation of the needles which interlock the particles, the ion-ion correlations are still present.
A very detailed calculation of the ion-ion correlations is given in Jönsson et al. [91]. The main conclusion thez draw is, that the presence of divalent counterions and a high surface charge density (high pH) are the main parameters influencing cement cohesion. Ion with higher valencies (e.g. Calcium ions) are needed for the coagulation. Trivalent cations are usually not present in

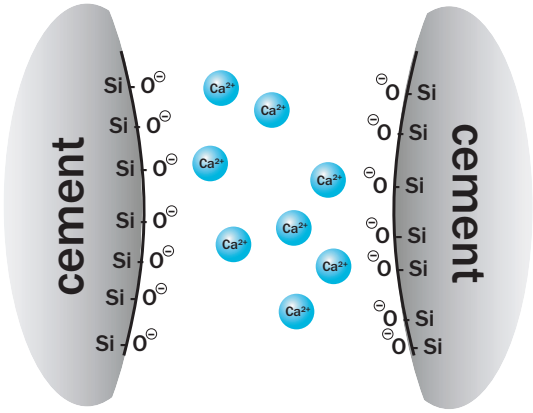

Fig. 2.17: Surface charges and ion-ion correlations between two CSH nanoparticles.

the solution since they are either amphoteric (Al(III)), or precipitate as insoluble hydroxides. The competition between monovalent (sodium, potassium) and divalent ions for the surface has the largest influence on the coagulation. The exact structure of the CSH phase is still debated [92] but it is believed to be strongly dependent on the C/S ratio in the clinker. The surface of the CSH nanoparticles can be negatively charged by —$SiO^{\ominus}$ groups, or positively by binding a divalent calcium ion as —$SiOCa^{\oplus}$. The bulk structure is build up by repeating "Dreierketten" of silicon oxide tetrahedral with parallel CaO plains. The surface structure has been imaged with the AFM at atomic resolution. Four different surface cells have been identified [93], with cell dimensions of a = 9.6 - 11.7 Å, b = 4.9 - 5.7 Å and α = 91 - 103°, depending of the C/S ration respectively.

2.6.2 Superplasticizers

Superplasticizers are used as an additive in cement. They decrease the viscosity of the cement paste and ensure a water like flow behavior [94]. This effect is used for easier transportation of the cement, to give the cement a specific form, or to ensure that a surface is smooth and planar.
Generally the cement paste can also be modified in its flow behavior by increasing the amount of water used in the paste. But since only a finite amount of water can be used for the hydration of the clinker, the excess amount will

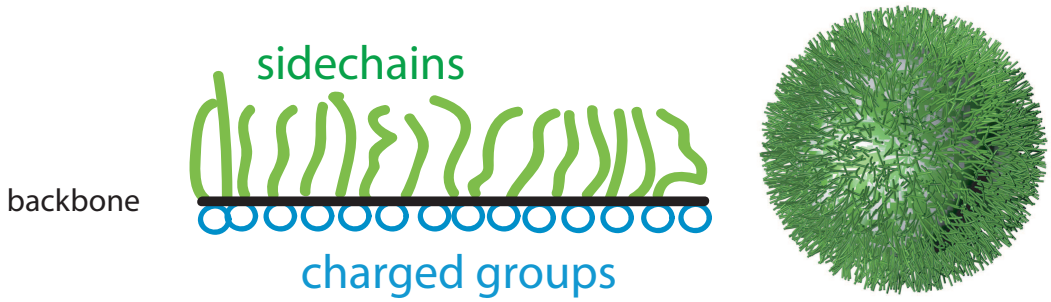

Fig. 2.19: Left: Scheme of a superplasticizer indicating sidechains (green), backbone (black) and carboxyl groups (blue). Right: CSH particle covered by superplasticizer. The sidechains protrude into the solution, but may also have a coil formation and not a stretched.

still be present in small cavities in the hardened cement and thus reduce the final strength and durability of the cement by precipitating and thus increasing the porosity.

Fig. 2.18: Excess water stays in the final hardened cement and reduces durability and strength.

Superplasticizers are copolymers with a backbone and sidechains (Fig.2.19). The backbone is mostly build from methacrylate or similar structures with a carboxyl group. At high pH, the carboxyl group dissociates and is negatively charged. It forms an immobile polymer layer at the interface of the nanoparticles due to the ion-ion correlations. The sidechains mostly consist of a linear polymer (e.g. polyethylene oxide) and are not charged. They protrude into the solution and give rise to a repulsive force between the CSH particles arising from the steric repulsion (Fig. 2.19). Generally, the adhesion to the CSH is controlled by the backbone, and the magnitude of the repulsion is controlled by the sidechains. If the superplasticizer is added and mixed with the cement paste, this becomes immediately liquid. However, after some minutes, the particles aggregate again, presumably due to the new growth of CSH needles, breaking up the polymer layer. Remixing of the paste redistributes the superplastsizer and the closed up polymer layer ensures again the water-like flow behavior.

The superplasticizers loose their effect after the first hour when the intercalation of the needles dominates the aggregation and solidification process.

2.6.3 Investigation of cement cohesion using the AFM

The focus of interest in studying cement cohesion is the structure of the CSH phase which controls the coagulation and hardening process and the surface forces acting between the CSH particles, which are responsible for the first stage of aggregation. The AFM is an unique tool enabling to a) image CSH surfaces at various resolutions and thus characterize the CSH structure from the micrometer to the Ångström scale and to b) measure surface forces between CSH particles under various conditions, such as ion concentration, surface charges and additives such as superplasticizers.
There have been several studies where the AFM was used to image the CSH surface [88,92,93,95–97] and where surface interactions have been measured [93,95,98]. The interactions are usually measured between pure CSH phases and not in a complex cement paste. Additionally Kauppi et al. [99] measured interactions between MgO surface and MgO particle. Using this setup, they managed to measure steric repulsion in a system with an adsorbed anionic acrylic esther-ethylene oxide. This showed nicely the difference between the adhesion in the pure system and the repulsion by adding a superplasticizer, which works similar for the MgO than for CSH.
Although the experimental conditions for an AFM are widely variable, the complexity of a cement paste is difficult to establish a reliable experimental setup. First, the ongoing reactions in a paste make the system too unstable (drift, surface precipitation), for a reliable AFM experiment. Secondly, the surface roughness is usually very large, which has a significant influence on the measured surface interactions, due to the ill defined contact area. Third, the carbon dioxide from the air induces carbonization in the cement paste, thus degrading the CSH phase. This effect is significant in an AFM experiment. The small amounts used, can be carbonized within hours.

3 Materials and Methods

3.1 Polymer Synthesis

1,4-Polyisoprene (PI) was synthesized from isoprene by anionic polymerization (Fig. 3.1). The isoprene was dissolved in freshly distilled cyclohexane and sec-butyl-lithium (BuLi) was added as a starter. After 12 h, the reaction was stopped with methanol (MeOH) and the product was recrystallized in tetrahydrofurane (THF). The purity of the polymer was verified using gel permeation chromatography (GPC).
The ratio of cis to trans was 70:30 as determined by NMR spectroscopy. By adjusting the amount of starter, PIs with molecular weights of M_w = 1.9-10.2 kDa where synthesized. This corresponds to mean end-to-end distances of 3 - 8 nm. To avoid oxidation, PI was stored in light protected flasks at -8°C. No change in the measured force curves for more than 16 h was observed, the oxidation in the AFM during measurements is therefore negligible. Additionaly a GPC was measured of samples older than 2 years, and these samples showed no oxidation.
Polydimethylsiloxane (PDMS) was synthesized from the trimer hexamethylcyclotrisiloxane by an anionic ring opening polymerization (Fig. 3.2). 10% of

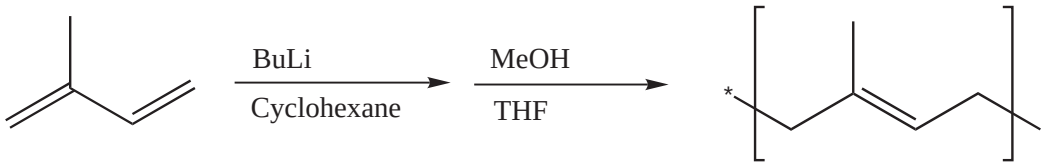

Fig. 3.1: PI was synthesized by anionic polymerization using sec-buthyl-lithium as a starter. The reaction was quenched after 12 h with methanol.

Polymer		$M_w / \frac{g}{mol}$	$M_n / \frac{g}{mol}$	Disp.	N	R_g / nm	$\eta / (Pa \cdot s)$
PDMS	PDMS6	5870	4220	1.38	79	2.0	0.052
	PDMS8	8380	7940	1.06	113	2.4	0.089
	PDMS17	16700	15900	1.05	226	3.4	
	PDMS19	18800	17500	1.05	254	3.6	0.360
PDMS-OH		19990	18700	1.07	270	3.8	
PI	PI2	1900	1652	1.15	28	1.4	
	PI3	2500	2270	1.10	50	1.9	0.68
	PI5	4800	4400	1.08	78	2.4	1.64
	PI7	6800	6400	1.06	100	2.7	2.94
	PI8	8000	7430	1.06	118	2.9	4.31
	PI10	10200	9800	1.04	150	3.3	7.70

Table 3.1: Overview of physical properties of the synthesized polymers. M_w, M_n and dispersity where measured with gel permeation chromatography, the viscosity with an ARES system, and R_g was calculated from the Kuhn lenght ($b_{PI} = 0.80nm$), and from the unperturbed radius of gyration $\frac{S_{0,z}}{M_w^{0.5}}[PDMS] = 266$ (Polymer Handbook)

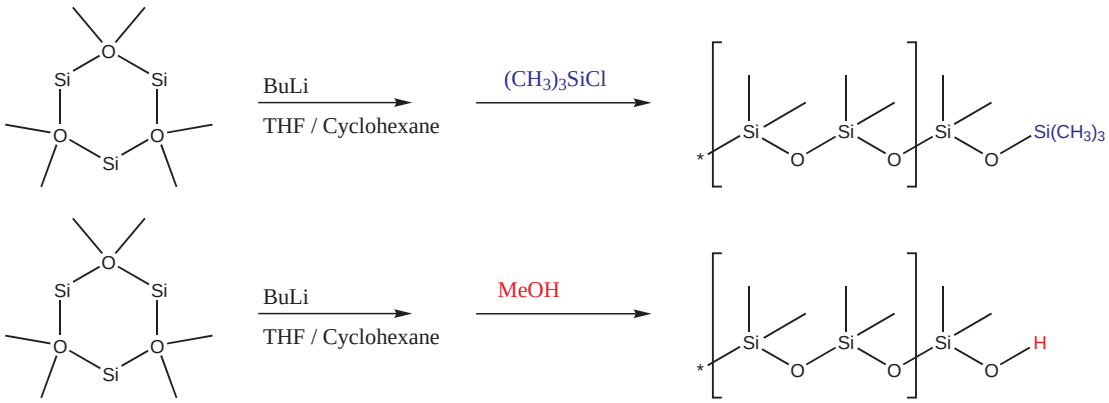

Fig. 3.2: Synthesis of PDMS. If the reaction is quenched with $(CH_3)_3SiCl$, the PDMS chain has two CH_3 endgroups. If the reaction is quenched with MeOH, one endgroup is a hydroxyl group.

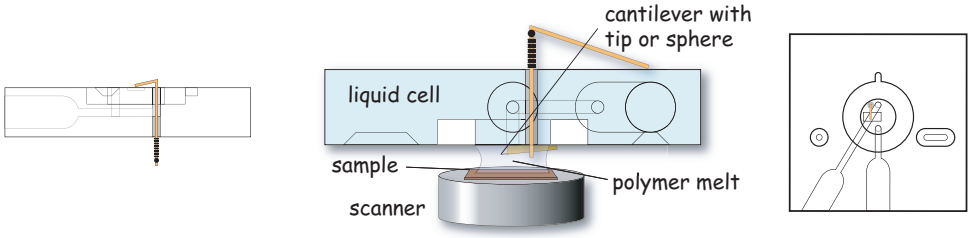

Fig. 3.3: Liquid cell for the AFM, used to measure in polymer melt. Left: sideview with the cantilever stage on top for mounting the cantilever), middle: cantilever mounted for measurement (upside down), right: top view.

the monomer was dissolved in freshly distilled cyclohexane and sec-butyllithium was added as a starter. After 10 h, the rest of the monomer was added in a THF/cyclohexane mixture (60:40). The reaction was stopped with $(CH_3)_3SiCl$ and the product purified with a fractionator. To keep the polymers water free, all samples were stored under vacuum and on molecular sieves.
Additionally, PDMS-OH was synthesized by stopping the reaction with Methanol.

3.2 AFM setup

All AFM measurements were carried out with a MultiMode with a Nanoscope IIIa controller (Veeco Instruments, Santa Barbara, CA) using a liquid cell without O-ring which was filled with the polymer melt (Fig. 3.3). The system was equilibrated for 10 h with the laser turned on to avoid drift caused by temperature differences or increased interaction forces caused by electrostatics due to the preparation process. The temperature inside the liquid cell was about 28°C during the measurements.
The silicon surfaces and cantilevers were plasma cleaned before each measurement for 5 min at 30 W in an argon atmosphere of 0.1-0.2 mbar. V-shaped cantilevers with silicon nitride tips (length 120 µm, width of each arm 18 µm, thickness 0.6 µm, Veeco Instruments, Santa Barbara, CA) were used. The radius of the tip curvature was determined from scanning electron microscope

(SEM) images (LEO 1530 Gemini, Oberkochen, Germany). A circle was fitted to the edges of the tip visible in the SEM image and the radius was calculated from the scale of the image. Typical radii of curvature were between $R = 10$ and 100 nm. Spring constants ranged from 0.2 to 0.6 N/m. For each experiment a new cantilever was used to avoid contamination with polymer from previous experiments.
To measure the hydrodynamic forces, the experimental setup was largely similar, except for two changes. First, instead of a sharp tip a particle was attached to a cantilever using epoxy resin as described below. Second, the force curves were measured with much higher velocity, ranging from 200 nm/s to 100 µm/s. Spring constants measured after attaching the particle did not change significantly and were still in the range 0.2 to 0.6 N/m.
For the experiments in polymer mixtures, the polymer melts have been mixed freshly before each measurement to a total amount of 200 µl. The fractions are always given in vol% with the short chain polymer first (short-vol% : long-vol%).

3.2.1 Cantilever Preparation

For hydrodynamic measurements, cantilever with an attached glass microsphere were used (borosilicate glass microspheres, 20 µm nominal diameter, Duke Scientific Corporation, Palo Alto, CA). The microspheres where attached on a tipless cantilever by using a micro manipulator (three dimensional oil-hydraulic manipulator MNO-203, Narishige Group, Japan) and epoxy resin (Epikote 1004, Shell, Germany) as glue. First some microspheres where distributed on a microscope slide so single particles could be seen in the microscope. Then small portions of epoxy resin were heated (80°C) next to the particles on the slide and the cantilever was dipped in the glue before picking up a glass particle using a micromanipulator [33, 34, 100–102].
The radii of the spheres where measured with the SEM and ranged from 9 to 11 µm. Before each measurement, the cantilever was plasma cleaned for 2 min at 30 W and 0.1 - 0.2 mbar, the spheres were cleaned for 30 seconds only.

3.2.2 Substrate Preparation

For most of the measurements silicon wafers (Wacker-Chemie, Burghausen, Germany) with an native oxide layer of approx. 2 nm were used. Before each measurement, they were plasma cleaned as mentioned before. Further samples were mica (Plano, Wetzlar, Germany) and highly oriented pyrolytic graphite (HOPG, SPI, West Chester, US) which were cleaved just before usage.

3.3 Measuring CSH interactions

3.3.1 Preparation of CSH surfaces

To get a sufficiently smooth CSH surface, preparation procedures of Plassard et al. [98] have been followed. A freshly cleaved calcite surface was immersed in sodium silicate solution ($[SiO_2]/[Na_2O] = 0.33$). In solution $CaCO_3$ is dissolved from the surface and CSH precipitated. After one week, the samples were transferred to CSH solutions, which have been prepared from saturated lime solution and additional CSH powder with a fixed C/S ratio. These solutions have been equilibrated for one week and filtered through a 0.22 µm Millipore filter. The samples stayed in these equilibrium solutions for one month. All steps have been done under argon atmosphere to avoid carbonization. The surfaces have been imaged in the AFM before their use in force curve measurements, and have been stored inside a glove box.

3.3.2 Preparation of CSH tips

For force measurements, triangular silicon nitride cantilevers with tip radii around 30 nm have been immersed in concentrated lime solution for 48 h. The silicon nitride cantilevers are covered with a native thin layer of silicon oxide ($\sim$ 5 nm) from which silicon ions dissolve into solution and reprecipitate as CSH on the apex of the tip (Fig.3.4). The reaction is automatically stopped after complete consumption of the silicon oxide layer.

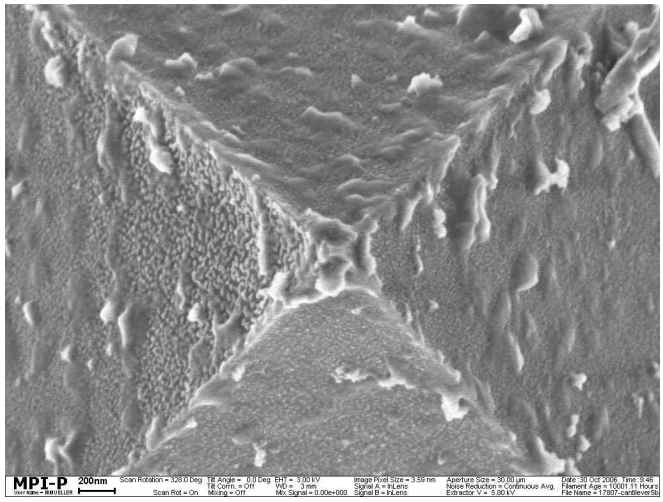

Fig. 3.4: Cantilever tip after immersion in lime solution for 48 h. The apex of the tip is covered with CSH crystals.

All tips have been imaged in the SEM after the measurements, to ensure the coverage of the apex with CSH. Spring constants have been measured before the CSH precipitation. It is mentioned at Plassard et al. [98] , that the CSH coverage changes the spring constant by less than 5%, which is caused by the change in mass.

3.3.3 Scaling with additional height

Measured distances in x and y directions are depending on the height of the sample [103]. This is usually negligible since most of the measured samples are less than 1 mm in height and the resulting error of measured distances is smaller than 2%, which is the standard error of an AFM.
The distortion is a result from the movement of the scanner, which is controlled by applying a voltage to the piezo, which bends the piezo in x and y directions. Unfortunately, the movement is not linear with the voltage, and the bending caused the sample to move on an arc (this can be seen as a rotation around the center of the piezo crystal) (Fig. 3.5, left). Therefore, scanners are calibrated by scanning a grid with indents of defined sizes and depths, thus adjusting the voltage to move the scanner surface along a specific dis-

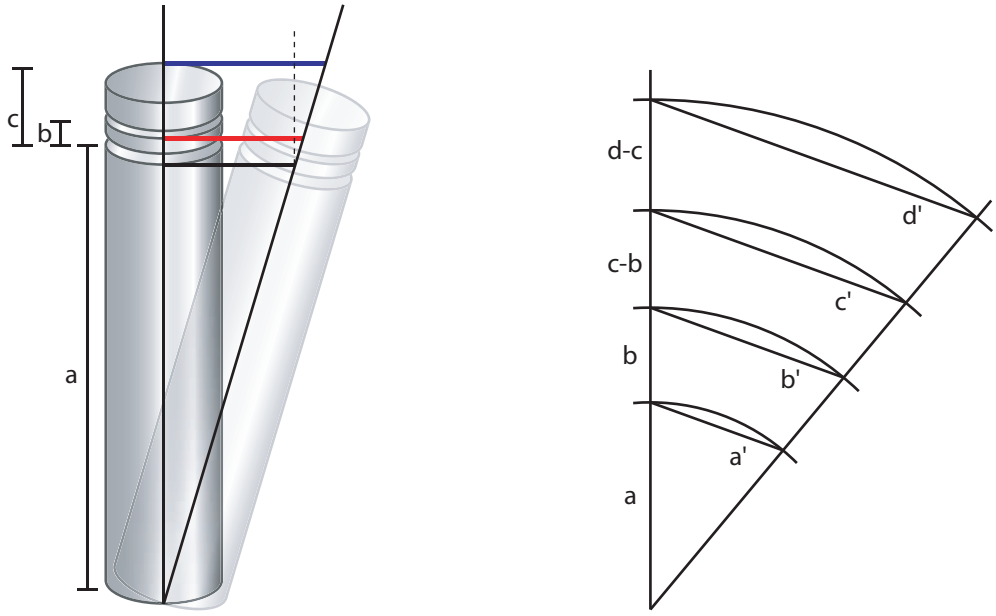

Fig. 3.5: Left: Due to the rotation of the scanner, samples with large heights result in too large values for x and y scales. Right: The distortion of the scale can be easily calculated by the theorem of intersecting lines.

tance.

If the sample is higher than a few millimeters, the bending of the piezo is still the same, but the sample surface is now further away from the rotation center, and is therefore moved a longer distance.

Instead of calibrating the scanner for different heights of samples, it is more convenient to measure the calibration grid at different heights, and calculate an elongation factor. This can be easily done with the theorem of intersecting lines, provided the increase in distance scales linearly with the additional sample height (Fig. 3.5, right). The theorem states the following:

$$\frac{a}{a'} = \frac{a+b}{b'} + \frac{a+c}{c'} + \cdots. \tag{3.1}$$

By eliminating a which is the unknown length of the piezo this results in:

$$-\frac{ba'}{-b'-a'} = -\frac{bc'-cb'}{c'-b'} \Rightarrow c' = \frac{ba'+cb'-ca'}{b}, \tag{3.2}$$

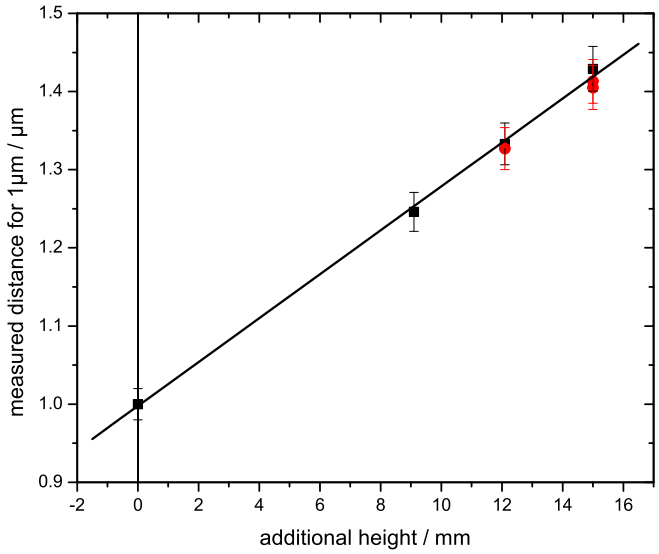

Fig. 3.6: The elongation factor of the scanner is the slope of the "measured distance" vs. "additional height" graph. Different data points are determined by different sets of the theorem of intersecting lines.

with the error:

$$\Delta c' = \frac{\partial c'}{\partial a'}\Delta a' + \frac{\partial c'}{\partial b'}\Delta b'. \tag{3.3}$$

By measuring distances a', b' and c' for different sample heights results in a measured distance vs. additional height graph showing a linear increase of the distortion with the additional height. The data for several different heights shows an error off less than 3% (Fig. 3.6).
The linear fit of the data gives a correction factor $k_{distort} = 0.028 \cdot \Delta h + 1\mu m$. All images measured at a certain additional height Δh have to be multiplied with $k_{distort}$ in x- and y-scales.

3.3.4 Determining lattice constants

Imaging the surface

AFM images of the surface have been taken in lime solution to minimize the surface interactions by excluding capillary* force and using a tip with a radius < 10 nm. Best resolution was achieved in friction mode with scan speeds of 30 Hz (per scanline). Before the measurement, the setup was allowed to equilibrate for 3 - 5 hours to minimize drift.
Since the measurement is very sensitive to noise, the resolution of the AFM was tested using the noise test procedure from the "Basic SPM Training Course" manual. After approaching the surface, the scan size is reduced to 1 nm. This ensures that the tip stays at the same point of the surface and only the noise is recorded. Then a 512 lines image is captured with a speed of 2 Hz. The image is then flattened and the root mean square (RMS) roughness is calculated. To achieve atomic resolution in the experiments, the RMS value should be below 0.5 Å.
The MultiMode AFM was tested before assembling the final experimental setup. The RMS value was at 0.4 Å. Then the MultiMode was transferred into a glovebox and the RMS value was measured again. The glovebox is important to exclude carbonation of the sample surface and can therefore not be avoided. Inside the glovebox, the RMS noise increased to ca. 1 nm. Possible reasons for this could be the higher pressure and the resonance of the glovebox due to external noise.

Calculation of the lattice constants

Two-dimensional AFM images give information about the lattice type (hexagonal, rectangular, etc.), lattice dimensions, and whether one or more lattices occurred. Before the analysis, the images were flattened, 2D fast Fourier transformation (2DFFT) was calculated, and the x and y coordinates of the inner spots were measured. To correct the drift of the AFM, the y positions of up- and down-scans should be averaged [104], but due to the low resolu-

*The capillary force arises from water which condensed into the gap between tip and surface. The capillary forces draw the tip and surface together and are therefore attractive.

Superplasticizer	M_w / kDa	M_n / kDa	PEO / kDa	R_g / nm
SP500	17	8	0.5	0.67
SP3000	35	17	3	1.64
SP6000	55	28	6	2.32

Table 3.2: Superplasticizers used in the AFM experiments. The PEO/kDa column gives the molecular weight of the sidechains only. R_g values are calculated for the PEO sidechain from $r_0/M_w^{0.5} \cdot 10^4 = 775$ (Polymer Handbook)

tion in the glovebox, and to the drift during the measurements, this was not possible. Therefore, the error of the calculated lattice constants is increased. From the measured distance in the Fourier image, the lattice constants are then calculated by:

$$d_a = l_a \cdot \sin\gamma, \quad d_b = l_b \cdot \sin\gamma, \quad d_c = \frac{l_a l_b \cdot \sin\gamma}{\sqrt{l_a^2 + l_b^2 - 2 l_a l_b \cdot \cos\gamma}} \tag{3.4}$$

If the lattice is hexagonal, the constants are simply

$$a = \frac{d_a + d_b + d_c}{3 \cdot \sin 60^\circ} \tag{3.5}$$

All the calculations have been performed by the SPIP Software (Image Metrology A/S, Lyngby, Denmark).

3.3.5 Superplasticizers

Three different superplasticizers were synthesized by BASF (Trostberg, Germany) (Tab. 3.2). They are copolymers with a methacrylate backbone and polyethylene oxide sidechains.

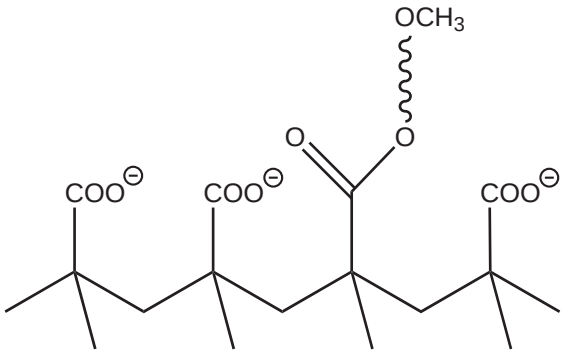

Fig. 3.7: The superplastiziser used have a methacrylate backbone and randomly distributed polyethylene oxide sidechains. The backbone has negative charges at pH 13 due to the carboxyl groups. The sidechains prodrude into the solution. The superplaticizers were synthesized at BASF, Torstberg.

4 Results and Discussion

The experiments discussed in this section cover three different systems: First, pure polymer melts of PDMS and PI measured on different surfaces. This was done in so called "quasi-static" experiments, using slow approaching / retracting velocities so the viscous drag has no effect on the measured forces, and in hydrodynamic experiments, where a borosilicate sphere was attached to the cantilever and the velocities were increased so the hydrodynamic forces dominated. The measurements are followed by a discussion if a solidification of the polymer layer occurs during the experiment. Second, the pure PDMS melts have been mixed to obtain a blend of homopolymer with two different chain lengths. The dependence of the layer formation on the molecular weight, which was investigated beforehand [24–26], makes it possible to distinguish short or long chain enrichment at the surface. Third, the effect of a superplasticizer in the gap between two CSH crystals in a CSH equilibrium solution at 0.1-vol.%. The focus of these experiments was to detect the surface forces in dependence of the molecular weight of the PEO side chains of the superplasticizer.

4.1 Pure polymer melts

4.1.1 Quasi-Static measurements

The presence, stability and thickness of a surface layer in a polymer melt can be most directly measured by its steric interaction with the tip. If a layer is formed, the interaction is repulsive and can be expected to increase with molecular weight. If no layer is formed, the entropy loss in the gap between tip and surface should force the polymer to move out of the gap, thus creating

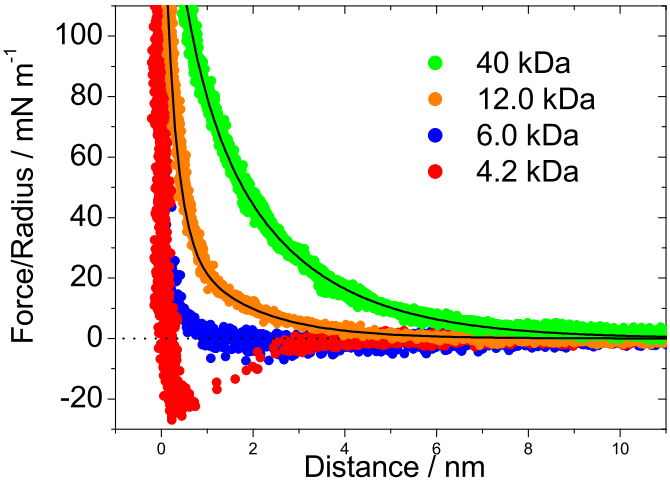

Fig. 4.1: Force-vs-distance curves in PDMS with different molecular weights (only approaching part shown). For small molecular weights attractive forces were observed, above 6 kDa, the interaction was repulsive and increased with molecular weight.

an attractive force on the tip [4].

Experiments in PDMS melt in dependence of the molecular weight have been done by Sun et al. [24–26]. A typical result is shown in Fig. 4.1, which displays an overlay of 30 approaching parts of force curves measured with a V-shaped silicon nitride tip with a radius around 30 nm and a spring constant around 0.2 N/m on a silicon oxide surface. To account for different tip radii and the resulting change in contact area, the measured forces have been normalized by dividing the tip radius. Approaching speeds were in the order of 50 to 500 nm/s and force curves have been taken on at least three different position on the sample. In all cases, the force curves showed no dependency of velocity or surface area. These factors are therefore neglected in the following discussions.

The force curves show a repulsion for 6 kDa and polymers with larger molecular weights, were for 4.2 kDa the interaction is purely attractive. Increasing the molecular weight above 6 kDa increases the repulsive force as well. The

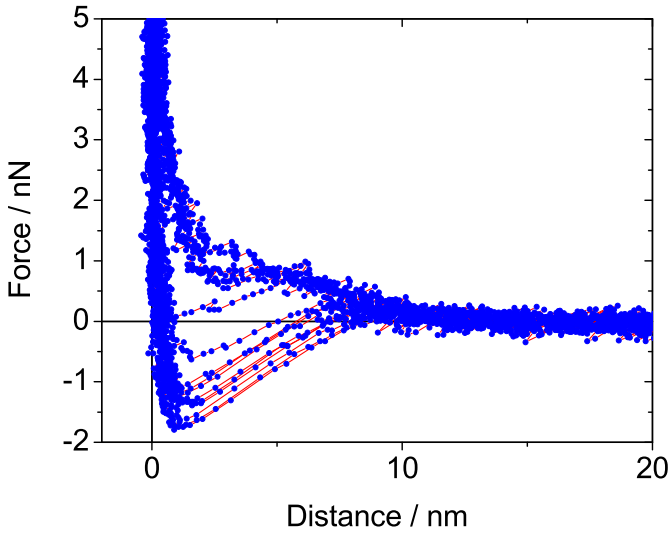

Fig. 4.2: Force curves in 8 kDa PDMS. Attraction was observed for high loads on the surface (> 15 nN), repulsion for smaller loads.

repulsion was weaker and unstable for molecular weights between 6 and 12 kDa, which is just below the molecular entanglement weight for PDMS (M_e = 12 kDa [27]). Apparently a minimum of entanglement of the polymer chains is necessary to form a stable surface layer. The formation of a more weakly attached layer even below the molecular entanglement weight is also possible, but this layer can be easily destroyed by an AFM tip.

To get more information about the stability of the layer close to the molecular entanglement weight, PDMS with 8 kDa has been investigated. As shown for 6 kDa PDMS, also for 8 kDa, a surface layer forms and it is possible to measure repulsive force curves. However, if the maximum load of the tip on the surface is increased above 15 nN, the repulsion changed to an attraction within 15 - 20 force curves taken every second (Fig. 4.2). During the same experiment, a repeated change of the load resulted in a repeated change of the surface forces. The layer is re-adsorbed after being destroyed by the tip. To show the range of forces present during the layer formation, fig. 4.2 was

not normalized with the radius. The re-occurrence of steric repulsive forces in this experiment took place in a matter of seconds. This indicates that the layer formation occurs in the same timescale, resulting in an equilibrium in less than a minute. This can change though, for higher molecular weights due to the increased entanglement. This might not necessarily increase the time to reach equilibrium, but might decrease it by adsorption of several already entangled coils from the melt.

For a quantitative comparison, normalized force curves were fitted with an exponential function according to $F = A_0 e^{-D/\lambda}$ (black lines). Here, F is the measured force, λ is the decay length, and A_0 is a prefactor. For PDMS, the decay lengths were $(0.58 \pm 0.12) R_g$ [25]. The decay length yields information about the range of the repulsive force, and hence convenient to compare the interaction between different molecular weights. It is not equivalent to the layer thickness.

Stable PDMS layers were found earlier for thermally treated PDMS-silicon oxide systems [105]. For the present system it can be concluded, that an immobile surface layer forms for molecular weights larger than 6 kDa, which is weak at first, but becomes more stable with increasing molecular weight. It is possible to determine the presence of the layer by its steric repulsion in the force curves and quantify the repulsion by the decay length.

Similar experiments were done in PI (M_e = 6 kDa) [27]. The measured forces were always repulsive, weak and short-ranged. The repulsion in the approach was much smaller than for PDMS (Fig. 4.3B) and also much less weight dependent (Fig. 4.1), resulting in decay lengths of typically 0.8 - 1.0 nm at M_w= 1.9 kDa and 0.3 - 0.6 nm for 6.8 kDa. The inset in fig. 4.3A shows the decay lengths for all molecular weights from 2 to 10 kDa on silicon oxide (orange). A tendency towards smaller decay lengths for increasing molecular weights was observed, which is the opposite trend to the observations for PDMS.

Forces on HOPG and mica where likewise repulsive and they showed similar decay lengths, though they were consistently weaker by a factor 2 - 3 than on silicon oxide (Fig. 4.4), although the contact angle of PI on HOPG is lower than on silicon oxide, and on mica is larger than on silicon oxide.

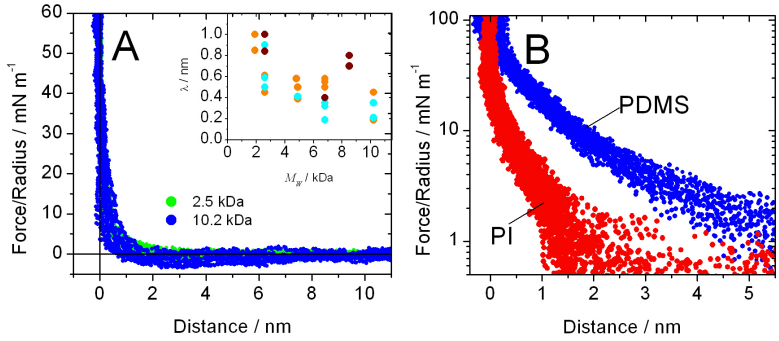

Fig. 4.3: A) Approaching force curves measured in PI on a silicon wafer with a silicon nitride tip. The inset shows the decay lengths from experiments on silicon wafers (orange), HOPG (cyan), and mica (dark red) are plotted. B) Approaching force curves measured in PI in logarithmic scale compared to force curves measured in PDMS (M_w = 18 kDa) on silicon oxide.

This trend of weaker surface interaction with increasing molecular weight is similar for measurements on HOPG and mica (Fig. 4.3A, inset). At higher molecular weight, in particular at M_w= 10.2 kDa, the repulsive force was often almost undetectable.

In theoretical calculations and computer simulations, it was found, that long flexible chains do not cause a strong surface interaction. Only if the chains are pinned to the surface a repulsive force is present which scales with the radius of gyration [2–4, 7]. Following this, we can say that PDMS forms an immobile surface layer, while PI does not. There are several possible reasons for this. One is, that the PI segments bind very weakly and are detached fast enough that no entanglements are present, which can form a stable layer. A second is, that the formation is too slow for a layer to rebuild after penetration with the AFM tip. A third is, that the PI chains can be easily moved laterally on the surface. The activation barrier for lateral movement of bonds might be much lower than for desorption. With the AFM it is not possible to distinguish, whether one or all three models contribute to the measured surface interactions. Implying similar formation timescales for PI and PDMS, we can only assume that the entanglements and the activation barrier for lateral

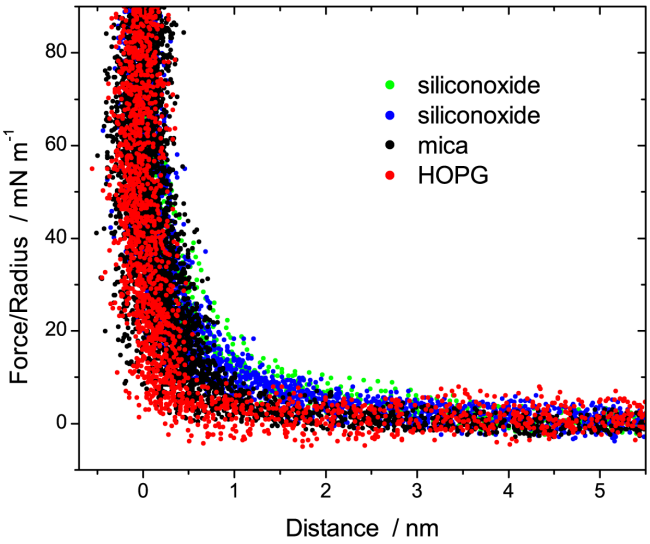

Fig. 4.4: Approaching force curves in PI on different surfaces. The interaction for mica and HOPG is weaker than for silicon oxide although the contact angle of PI on HOPG is lower than on a silicon oxide, and, on mica is larger than on silicon oxide.

movement is of greater importance.

We called the experiments described above "quasi-static" experiments because the forces were independent of the approaching/retracting velocities and we assume that viscous drag had no influence on the approaching force curves. There is one restriction, which is not relevant with respect to confined polymers, but with respect to the technique of AFM force measurements: In many experiments we observed an apparent strong repulsion in the retracting parts of force curves (Fig. 4.5). This repulsion increased with retracting velocity. This is attributed to the hydrodynamic drag on the cantilever. When the cantilever is retracted the tip is still in contact with the sample surface. Thus, the velocity of the tip is zero, while the back end of the cantilever is already moving with its constant retracting velocity v_0. Only when the tip is released from the surface the front end of the cantilever starts to move. Due to the damping of the viscous liquid it reaches its final retracting velocity v_0 only after a delay. This implies, that the hydrodynamic force on the cantilever is not constant, but increases with time. Since for the calibration the hydrodynamic drag on the cantilever is assumed to be constant, this effect is not

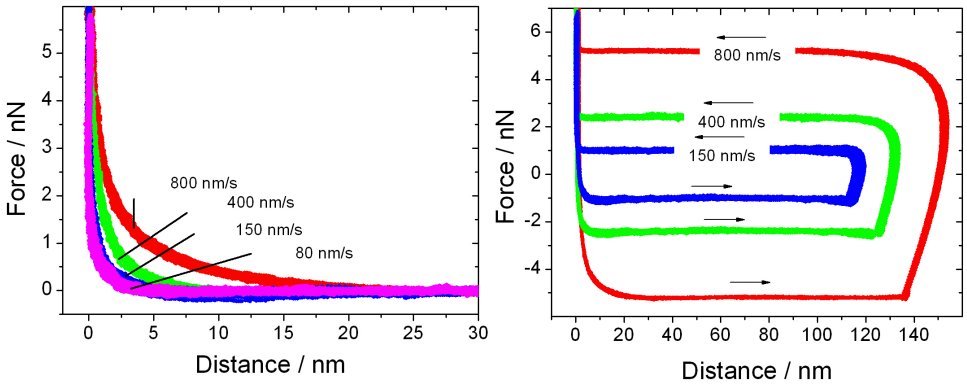

Fig. 4.5: Left: Retraction force curves with a V-shaped silicon nitride tip (R $\approx$ 30 nm, k_c = 0.2 N/m) on a silicon oxide surface in 4.8 kDa PI. The viscous drag on the cantilever depends on the velocity. Right: Approach and retract of the force curves.

taken into account. This becomes apparent in the retractive force curves if the viscous drag exceeds a certain value. The effect is proportional to $v_0\eta$. To avoid this effect the calibration procedure for retracting force curves was only done for $v_0\eta \ll 10^{-7}$ N/m.

4.1.2 Hydrodynamic measurements

The formation of an immobile surface layer does not only result in a steric repulsion. The flow of the polymer over the surface also depends on the surface properties and might - for a non-Newtonian fluid - show surface slip. With the formation of a surface layer, the surface properties are changed and it should be possible to observe this change also in the surface slip. Using the AFM, this can be done in hydrodynamic measurements using a borosilicate glass sphere with a diameter of 10 µm and using approaching speeds of 1 - 100 µm/s.

Hydrodynamic force curves where measured in PDMS and PI at three different molecular weights each (Fig. 4.6 and 4.7). Displayed are again overlays of approaching parts of ca. 30 force curves for each of the three graphs. Due

to the relative small variance in the particle radius, the force curves have not been normalized.
As it can be seen, a long-range repulsive force was present, which decreased with distance, plus a constant, distance-independent component. The distance-independent component is caused by the drag on the cantilever. The long-range decaying force is due to the fact that the polymer melt has to be squeezed out of the closing gap between the planar substrate surface and the microsphere. Both components increased with the approaching velocity v_0 and with the viscosity of the melt. To determine the presence of slip, the transition into contact at zero distance is important. If no slip is present, the velocity of the microsphere decreases smoothly to zero until contacting the surface, while with slip the velocity on the surface is still finite and a kink appears in the force curves. Since these kinks can be small, it is not always easy to determine the presence of slip from the force curves alone. Therefore we additionally calculated velocity curves, by differentiating deflection-vs-time plots. The velocity is then plotted vs the distance and we briefly call the curves "velocity curves". In these plots, the slip becomes apparent by an interception of the velocity axis larger than zero.
All force curves where fitted with the model described by Vinogradova [72] earlier (see section 2.3.2). The fits are displayed in the graphs (4.6, 4.7) as grey lines. The Hamaker constant was estimated to be around $2 \cdot 10^{-21}$ J, but the contribution of the van der Waals forces turned out to be negligible compared to the hydrodynamic forces under our experimental conditions.

Polyisoprene

The results are dependent on the molecular weight (Fig. 4.6). For **PI3** (η = 0.60 Pa·s) the fit showed good agreement with the measurement up to the highest approaching velocity of 5 µm/s. The slip lengths required to obtain the best fit were 5 - 10 nm, independent of the approaching velocity. Slip was neither directly visible in the measured force curves nor in the velocity curve. For **PI5** (η = 1.64 Pa·s) the curves could not be fitted with any hydrodynamic model if we used bulk viscosities. To obtain an agreement between simulated

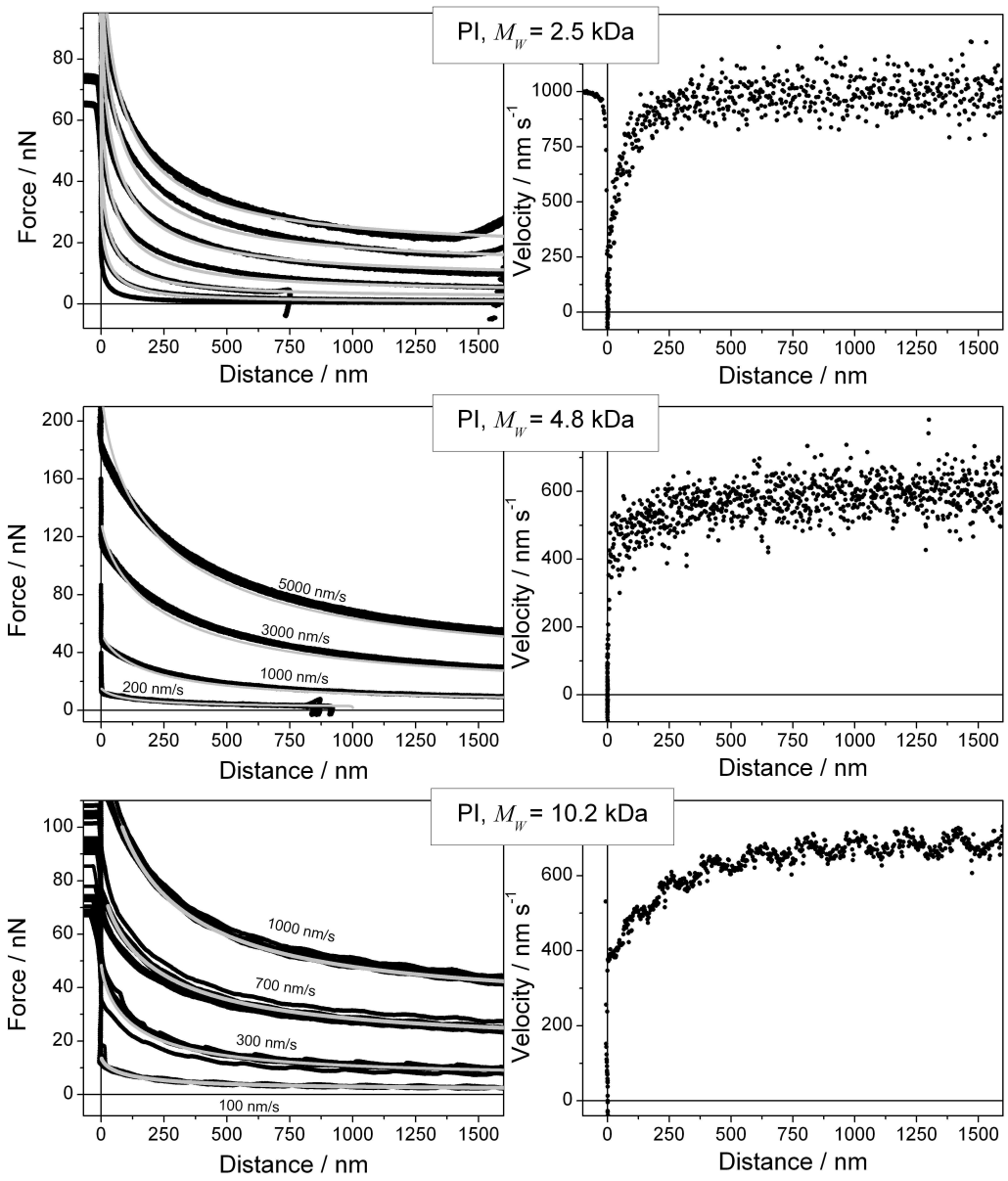

Fig. 4.6: Hydrodynamic force (left) and velocity (right) curves measured on silicon wafers with glass microspheres at different approaching velocities in PI. Only approaching parts are shown. The experimental results are fitted by a hydrodynamic simulations including slip (gray lines). Top: PI3, k_c = 0.27 N/m, R = 10.8 µm, η = 0.7 Pa·s at approaching velocities v_0 = 0.2, 0.5, 1, 2, 3, 4, and 5 mm/s (bottom to top curve). The velocity curve was recorded at v_0 = 1000 nm/s. Slip lengths of b = 5 - 10 nm were used for the fit. Middle: PI5, k_c = 0.26 N/m, R = 11.0 µm, η = 4.0 Pa·s at approaching velocities v_0 = 0.2, 1, 3, and 5 µm/s. The velocity curve was recorded at v_0 = 600 nm/s. Slip length of b = 30 - 100 nm were used for the fit. Bottom: PI10, k_c = 0.27 N/m, R = 10.8 µm, η = 7.7 Pa·s, v_0 = 0.1, 0.3, 0.7, and 1 µm/s. The velocity curve was recorded at v_0 = 700 nm/s. Slip length of b = 30 - 80 nm were used for the fit.

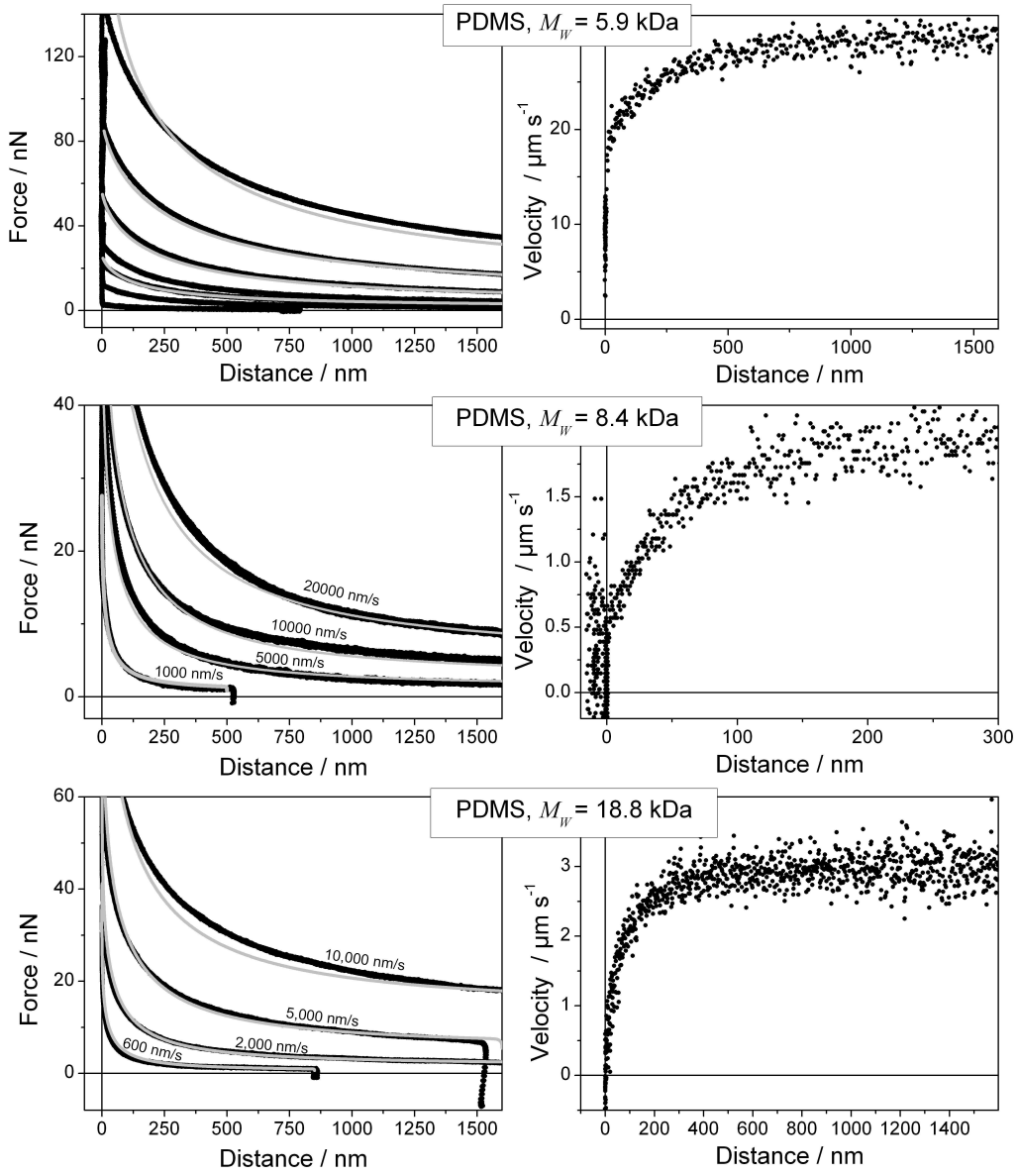

Fig. 4.7: Hydrodynamic force curves measured on silicon wafers with glass microspheres at different approaching velocities in poly(dimethyl siloxane) (PDMS). Only approaching parts are shown. Top: PDMS6, $k_c = 19$ N/m, $R = 9.1$ µm and $\eta = 0.22$ Pa·s at approaching velocities $v_0 = 1, 2, 5, 10, 15, 30, 60$ and 100 µm/s (bottom to top curve). Middle: PDMS8, $k_c = 0.27$ N/m, $R = 11.0$ µm and $\eta = 0.15$ Pa·s at $v_0 = 1, 5, 10$ and 20 µm/s. Bottom: PDMS19, $k_c = 0.24$ N/m, $R = 10.8$ µm and $\eta = 0.36$ Pa·s at approaching velocities $v_0 = 0.6, 2, 5$, and 10 µm/s. The experimental results (filled dots) are fitted by hydrodynamic simulations without slip (grey lines).

and experimental curves, a viscosity of 4.0 Pa·s had to be assumed, which is more than twice as high as the experimentally determined value. To explain this behavior, the possibility of changed viscosities is discussed in detail later. Slip is identified by a kink in the force curves at the contact point. It becomes even more evident in the velocity curves. For $D \rightarrow 0$ the velocity still possesses a finite value. Slip lengths decreased from 100 nm at 200 nm/s approaching speed, to 30 nm at 5000 nm/s approaching speed.
An increased viscosity of confined polymer melts has been observed with the SFA as well [14, 17, 67]. Also the pressure increase in the gap between microsphere and planar surface, which can reach ≈1000 bar, can lead to an increase of the viscosity. Since the shear rates in the center of the gap between particle and surface are zero (this is discussed in detail later when also shear rate profiles are calculated), the confinement effect might be dominating in our experiments. For example, the zero shear viscosity of PDMS increases by one order of magnitude when increasing the pressure by ≈700 bar [106]. It might also be an indication that hydrodynamic forces in melts have to be described by a full viscoelastic theory.
High molecular weight PI (**PI10**, η = 7.7 Ps·s) force curves could again be fitted with a hydrodynamic force including slip. Slip lengths of 30 - 80 nm were found, again independent on the approaching velocity. Slip was visible in force curves and in velocity curves.

PDMS

Judging from results of contact angle measurements, the PDMS spreads fully on silicon oxide, therefore the interaction between the polymer and the solid surface should be stronger than for PI on silicon oxide. For high molecular weight PDMS (**PDMS19**), it was possible to fit the force curves without slip, according to equations 2.19 - 2.22. Only for velocities higher than $v_0 = 10$ µm/s, the experimental curve diverged to higher forces.
For a molecular weight of **PDMS8** the force curves did not show slip, velocity curves did. In contrast to higher molecular weights, the force curves could only be fitted assuming a viscosity of 0.15 Pa·s, which was three times larger

than experimental values, and no slip. The fits were in good agreement with the experimental curves up to 20 µm/s, which corresponds to $\eta v_0 = 3.0 \cdot 10^{-6}$ N/m.
PDMS of low molecular weight (**PDMS6**) could only be fitted with a viscosity of 0.22 Pa·s, which is four times higher than the bulk viscosity, and a slip length of 70 nm. Slip was evident in force curves and velocity curves, but like for PI5 and PDMS8, the viscosity had to be increased by a factor of two to four to get agreement between experimental and simulated curves. Assuming increased viscosity, fitting was possible up to 60 µm/s. For 100 µm/s the experimental curve diverged to higher forces.

Possible Artifacts

There are two important sources of possible artifacts in force curve measurements which need to be considered. Surface asperities between microsphere and solid surface can prevent full contact of the two surfaces, thus falsifying the interpretation of zero distance. If contact is established by an asperity and not the real surface of the sphere or the surface, the measured zero-distance-velocities will be too large and the zero-distance-forces too small, which then would result in a false prediction of boundary slip. To verify that asperities did not influence the results we imaged the surfaces and reversely imaged the particles with a grid of sharp tips (µmasch tip characterization grid TGT01 (Anfatec,Oelsnitz, Germany) as described in refs. [107–109], with an AFM (Fig.4.8). In our experiments the substrate used and the particle surface were smooth and showed no asperities. Measured root mean square (RMS) roughnesses over 1 µm^2 on sphere and flat surface were typically 0.27 nm for the surface and 4 nm for the sphere.
The second effect to consider is the change of the hydrodynamic force close to the surface. When the microsphere approaches the planar surface its velocity is gradually reduced until it is zero. This does not only reduce the hydrodynamic drag on the microsphere, but on the cantilever as well. Different parts of the cantilever are differently affected. The base of the cantilever, close to the chip, is only weakly affected because it moves with a velocity close to

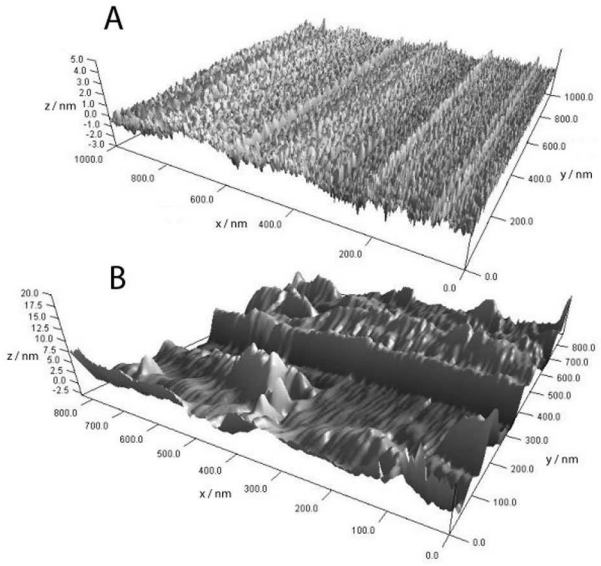

Fig. 4.8: Flattened images of A: the silicon oxide surface and B: the borosilicate particle. The flattening of the image of the particle was done including a spherical geometry.

v_0. The end of the cantilever, where the microsphere is attached and which dominates the total interaction [110], is strongly affected because here the velocity reduction is significant. To quantify this effect we replaced the constant hydrodynamic force term in eq. (2.19) by

$$F_{drag} = \alpha \frac{1}{v_0} \left| \frac{dD}{dt} \right| F_0 + (1 - \alpha) F_0 \tag{4.1}$$

Here, F_0 is the drag on the cantilever acting if all parts are moving with v_0 and α is the contribution of the end of the cantilever. Hydrodynamic force curves simulated with eq. 4.1 are indeed influenced by the drag force on the cantilever (Fig. 4.9). This influence is, however, small. The effect of slip will dominate. Only for slip lengths $b < 10$ nm the influence should be considered.

Slip

Considering these possible sources of misinterpretation of hydrodynamic force curves, the experimental results indicate the occurrence of boundary

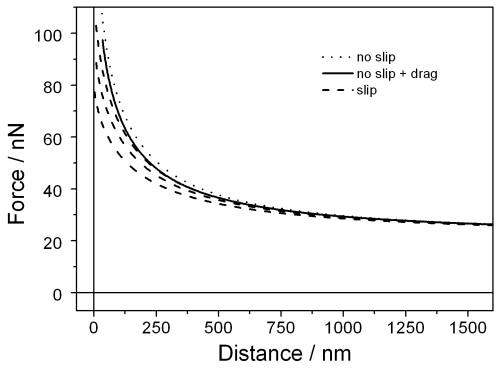

Fig. 4.9: Simulation results for hydrodynamic force curves, with R = 10 µm, v_0 = 5 µm/s, k_c = 0.26 N/m, L = 120 µm, w = 36 µm, η= 0.6 Pa·s, and F_{drag} = 13 nN. No slip (dotted), no slip and taking the varying drag on the cantilever into account according to eq. (4.1) with α = 1 and F_0 = 13 nN (continuous line), and slip of b = 20, 40, and 80 nm (dashed, from top to bottom). For the dashed curves F_{drag} = 13 nN and α = 0.

Polymer	M_w/kDa	FC	VC	slip length
PDMS19	18.8	no	no	-
PDMS9	8.4	no	yes	-
PDMS5	5.2	yes	yes	70
PI10	10.2	yes	yes	30 - 80
PI5	4.8	yes	yes	30 - 100
PI3	2.5	fit only	no	5 - 10

Table 4.1: Overview of the results of the hydrodynamic measurements. FC: slip evident in force curves, VC: slip evident in velocity curves.

slip in all cases, with the exception of PDMS19 (Tab. 4.1). In most cases slip is directly evident (PI5, PI10, PDMS6), in other cases only the fit revealed slip (PI3, PDMS8). There are three different ways to interpret slip:
(1) The velocity of the polymer melt at the solid surface or in a shear plane close to the solid surface is not zero and a freely moving melt is "slipping" over the solid surface, or over a layer bound to the solid.
(2) The viscosity of the melt close to the solid surface is reduced with respect to its bulk viscosity so that a steeper velocity gradient arises. An explanation for this could be shear thinning: The flow of the melt aligns the linear polymer chains and reduces the effective viscosity.
(3) AFM force measurements do not allow to determine the absolute value for zero distance between sphere and surface. Zero distance is assumed where the sphere stops moving, which is when hard contact is attained. It could happen that the normal pressure of the tip induces a phase change in the polymer so that it solidifies abruptly and the tip can not penetrate further. The polymer forms a solid surface layer and the "zero distance" measured by the AFM is instead several tenths of nanometers from the solid surface. To avoid confusion we would like to stress the difference to the immobilized layer mentioned earlier: The immobilized layer is always present, while a "solidifying" layer forms abruptly upon approach. The possibility of such a solidifying layer is discussed in more detail in section 4.1.3 where the Young's Modulus of such a layer is calculated and compared to the results.
If a solid layer is formed, it should be possible to fit the force curves by simply shifting the simulated curves by the thickness of the layer. This is attained by substituting the distance D in eq. (2.22) with a modified distance $\Delta D = D_L + D$, with D_L being the thickness of the solidified polymer layer, and then simulating the curve as before. The two different models ("slip length" and "curve shift") can both be used for correctly fitting the force curves, so that we are not able to discriminate between them. On the other hand we are able to discriminate between the two models in a velocity curve, by comparing to factors: The steepness of the velocity-vs-distance curve decreases close to the surface, and the contact velocity is larger than zero. Very close to the surface (< 5 nm), the results show agreement with the slip model: in fact

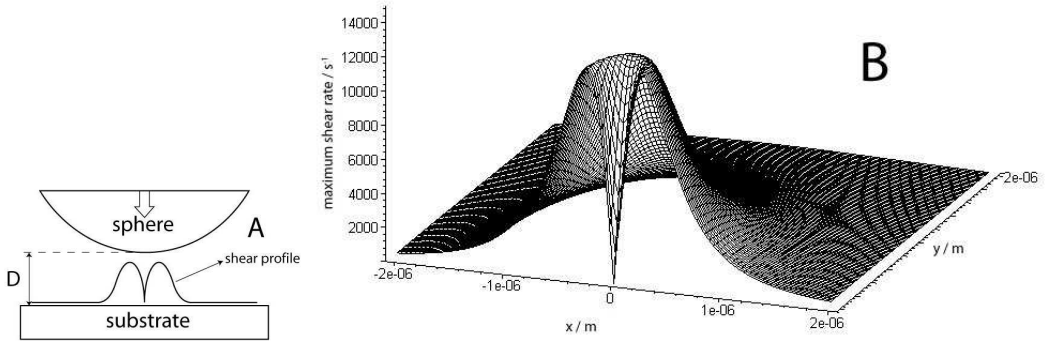

Fig. 4.10: A: Sketch of the shear rate profile in the gap between tip and surface for a specific distance D. B: Simulated maximum shear rates for η = 0.05 Pa·s, R = 10 mm, v_0 = 30 µm/s, D = 10 nm, without slip. The shear rates are plotted versus the lateral distance on the surface.

the contact velocities predicted by the slip model and that of the experiment are similar (Fig. 4.11), while the no-slip model and the curve shift model can not account for both: The shape of the experimental curve and the contact velocity. It should be noted that even though the fit supports the slip model, the differences are too small to allow ruling out completely the existence of a solidifying layer on the surface.

A typical profile of shear rates in the gap between particle and surface shows highest shear rates at a circle around the center of approach (Fig. 4.10). This profile depends on the distance between particle and surface and, assuming no slip, maximum shear rates approach infinity, for $D \rightarrow 0$. To calculate maximaum shear rates during the approach of the particle, we used [51]

$$\dot{\gamma}_{\max} = \frac{9\sqrt{2R}}{D^{2/3}\sqrt{3R}} \frac{dD}{dt} \tag{4.2}$$

This equation was derived for Newtonian liquids, where the velocity dD/dt depends linearly on the viscosity. It is not strictly valid for our experiments with polymers, where the viscosity might not be constant, but it can provide an estimation of the upper limit of occurring shear rates. To compare the force experiments, shear rates at a fixed distance $D = 10$ nm for $R = 10$ µm, $k_c = 0.27$ N/m, and $b = 0$ were calculated with Eq. (4.2) for each polymer at all measured velocities (Tab. 4.2).

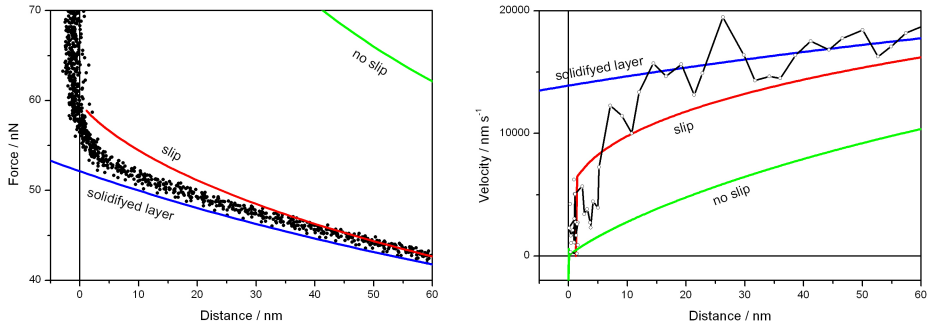

Fig. 4.11: Velocity curve (below) and force curve (above) for PDMS6, v_0 = 30 µm/s, R = 9.1 µm, k_c = 0.19 N/m, η = 0.22 Pa s. The experimental data has been fitted assuming no slip (green), assuming slip (red), and assuming a solid layer on the surface (blue).

Polymer	M_w/kDa	γ_{max}/s^{-1}
PDMS6	5.9	$2.5 \cdot 10^5$
PDMS8	8.4	$8 \cdot 10^4$
PDMS19	18.8	$3 \cdot 10^4$
PI3	2.5	$1.5 \cdot 10^4$
PI5	4.8	10^4
PI10	10.2	$2 \cdot 10^3$

Table 4.2: Maximum shear rates for all hydrodynamic measurements.

The highest shear rates occur with the PDMS, while force curves measured in PI where taken with a smaller approaching speed since its viscosity was higher.
For the fitting of PDMS6 and PDMS8 a 3 - 4 times higher viscosity was required. As mentioned before, the reason could be due to the high pressures of around 1000 bar. This argument seems reasonable for PDMS, since the increase in viscosity correlated with the higher shear rates. It is, however, still unclear, why an increased viscosity was only observed for PI5 and not for PI3, which was measured at a higher shear rate.

4.1.3 Young's Modulus of immobilized layers

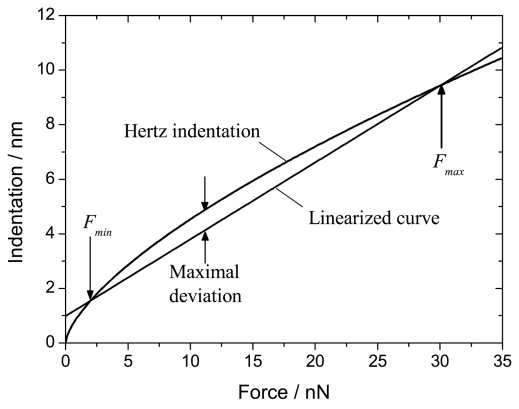

Fig. 4.12: Indentation in dependence of the applied force in a force curve. The graph shows the deviation from the linear force resulting from a soft layer on the surface calculated by the Hertz model.

To calculate Young's Modulus of a solid-like surface layer in an AFM experiment, a situation is considered where the tip is immersed in polymer solution with the solid support and the tip being infinitely hard. If the indentation of the layer δ is much smaller than the thickness D, the Hertz model gives the following equations to calculate the force-vs-indentation curve (see section 2.25):

$$F = \frac{4}{3} \cdot \frac{E}{1-\nu^2} \cdot \sqrt{R\delta^3} \quad \text{with} \quad \delta = \left[\frac{3}{4} \frac{F\left(1-\nu^2\right)}{E\sqrt{R}} \right]^{\frac{2}{3}} \tag{4.3}$$

Here, E is Young's modulus of the layer, R the tip radius, and ν is its Poisson ratio. Since for polymers $\nu \approx 0.3$ we have $1 - \nu^2 \approx 1$. For an AFM tip in contact with an elastic body the force increases as $F \sim \delta^{1.5}$, and not linearly. From the change in slope, or by fitting F-vs-δ curves Young's modulus can

be inferred. If the material is hard compared to the spring constant of the AFM cantilever, the difference between the indentation given by eq. 4.3 and a linear increase is small. In case of a soft material the deviation from the linear increase is significant.
To calculate the deviation from a linear force curve, we have to consider the minimal and maximal forces between which the force curves shows a linear increase. For a typical AFM experiment, this would be between 2 nN and 30 nN. Using the Hertz model for a force curve with indentation of the layer, and a linear force curve with the same start and end points

$$\delta = \alpha F_{\text{min}}^{2/3} + \alpha \cdot \frac{F_{\text{max}}^{2/3} - F_{\text{min}}^{2/3}}{F_{\text{max}} - F_{\text{min}}} \cdot (F - F_{\text{min}}) \quad \text{with} \quad \alpha = \left[\frac{3\left(1-\nu^2\right)}{4E\sqrt{R}} \right]^{\frac{2}{3}} \tag{4.4}$$

the difference given as

$$\Delta\delta = \alpha F_{min}^{2/3} + \alpha \cdot \frac{F_{max}^{2/3} - F_{min}^{2/3}}{F_{max} - F_{min}} \cdot (F - F_{min}) - \alpha F^{2/3} \tag{4.5}$$

and the maximum at

$$F = \frac{8}{27} \cdot \left(\frac{F_{max} - F_{min}}{F_{max}^{2/3} - F_{min}^{2/3}} \right)^3 \tag{4.6}$$

Inserting this into eq. 4.5 leads to

$$\frac{\Delta\delta}{\alpha} = F_{min}^{2/3} - \frac{F_{max}^{2/3} - F_{min}^{2/3}}{F_{max} - F_{min}} \cdot F_{min} - \frac{4}{27} \cdot \left(\frac{F_{max} - F_{min}}{F_{max}^{2/3} - F_{min}^{2/3}} \right)^2 \tag{4.7}$$

Now we can estimate a lower limit for Young's modulus. Due to noise we have an uncertainty of $\Delta\delta \approx 0.3$ nm. With $F_{min} = 2$ nN, $F_{max} = 30$ nN, and $R = 50$ nm we find $E > 4 \cdot 10^8$ Pa. Thus if an immobilized layer prevents the tip from getting into direct contact with the solid surface its Young's modulus must be higher than $4 \cdot 10^8$ Pa. For hydrodynamic experiments, $\Delta\delta$ and $F_{max} - F_{min}$ are increased due to the larger ramp size measured and the resulting smaller resolution at close distances. With values of $\Delta\delta \approx 2$ nm, $F_{min} =$

50 nN, $F_{max} = 100$ nN, and $R = 10$ µm we find $E > 4 \cdot 10^5$ Pa.
For lower Youngs's moduli, the force curve should show a significant deviation from linearity due to the compression of the polymer layer (Fig. 4.12). Since deviations are not visible in the experiments, and a Young's modulus of $4 \cdot 10^8$ Pa is very large even for a solidified polymer layer, it can be assumed that all polymer has been squeezed out of the gap rather than a polymer layer of such a high stiffness.
However the picture changes for the hydrodynamic experiments, where not only the minimal and maximal forces applied on the surface and the noise level of the force curve, but also the contact radius of sphere changed, and the contact area is much larger than with a silicon nitride tip. As a consequence the experiments show that Young's modulus has to be higher than $4 \cdot 10^5$ Pa, not to be indented by the particle. Layers with $E \geq 4 \cdot 10^5$ Pa could not be discriminated from perfectly rigid surfaces. This implies that in the case of hydrodynamic experiments, a polymer layer might still have been present during a hydrodynamic experiment and no real contact of sphere and hard surface was established.
For the solid foundation model, by using eq. 2.26 and $\beta = \sqrt{D/\pi ER}$ we get

$$\Delta\delta = \beta\sqrt{F_{min}} + \beta \cdot \frac{\sqrt{F_{max}} - \sqrt{F_{min}}}{F_{max} - F_{min}} \cdot (F - F_{min}) - \beta\sqrt{F} \tag{4.8}$$

this is maximal at

$$F = \frac{1}{4}\left(\frac{F_{max} - F_{min}}{\sqrt{F_{max}} - \sqrt{F_{min}}}\right)^2 \tag{4.9}$$

Inserting this into eq. 4.8 leads to

$$\frac{\Delta\delta}{\beta} = \sqrt{F_{min}} - \frac{1}{4}\frac{F_{max} - F_{min}}{\sqrt{F_{max}} - \sqrt{F_{min}}} - F_{min}\frac{\sqrt{F_{max}} - \sqrt{F_{min}}}{F_{max} - F_{min}} \tag{4.10}$$

Since the thickness of the hypothetical layer is unknown we can only give a lower limit for Young's modulus divided by the thickness. This is $E/D = 2.5 \cdot 10^{16} Pa/m$ for experiments with microfabricated tips and $E/D = 2.5 \cdot 10^{11} Pa/m$ for the hydrodynamic experiments. Thus, if a layer is still present between the AFM tip and the solid support, its Young's modulus divided by

the layer thickness is higher than $E/D = 2.5 \cdot 10^{16} Pa/m$. Unless the layer thickness is below 0.2 nm (in which case continuum models break down) the Hertz model is appropriate to calculate the lower limit of Young's modulus.
The experiments can be summarized to the facts that it was a) possible to detect the presence of an immobile surface layer via the change in the slip boundary condition, b) the magnitude of the slip increases with decreasing layer thickness and its stability and c) the opposite trend of layer formation for PDMS and PI was confirmed. However, the solidification of the polymer layer in hydrodynamic experiments can not be ruled out and should be considered as a source of artifacts.

4.2 Polymer mixtures

Polymer melts do not consist only of chains with the same chain length, but are always a mixture of homopolymers varying in chain length. Therefore homopolymers, although chemically identical, have different adsorption energies, due to the chain length dependent conformational entropy loss at the surface. Since it is possible to distinguish short and long chain dominance at the surface by taking force curves, a mixture of two homopolymers with different chain length was investigated with respect to the chain length differences and the volume fractions.
Force curves of PDMS show a repulsive force for high molecular weights (16.7, 18.8 and 19.9 kDa) which was attributed to the formation of a immobilized polymer layer on the surface. PDMS with a molecular weight below 8 kDa apparently does not form such a layer.
Looking at mixtures of different volume fraction (φ) of short and long PDMS, short chains should be enriched near the surface due to their smaller loss in entropy (see section 2.1.2), therefore no immobile surface layer should be formed and an attractive force is expected.
Force curves in a mixture of 5.9 and 18.8 kDa PDMS show indeed a short range attraction for short chain volume fraction from $\varphi_{short} = 1$ to 0.2 (Fig. 4.13 C - E). Only for volume fractions of $\varphi_{short} = 0.1$ and below, a repulsive

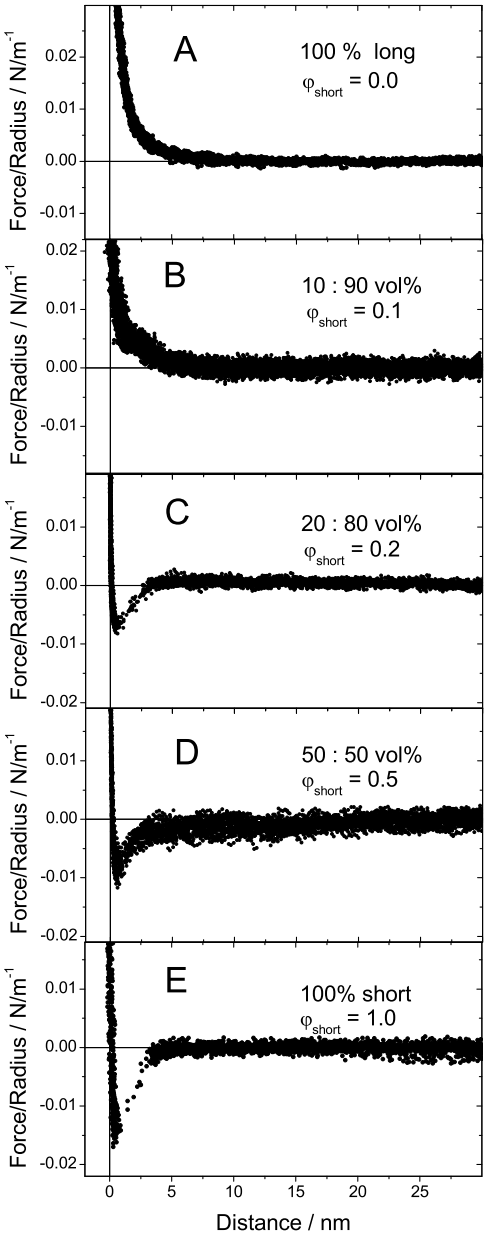

Fig. 4.13: Approaching force distance curves in mixtures of two PDMS melts with different chain lengths (5.9 kDa and 18.8 kDa). The graphs show force curves in the pure melts (A, E) and mixtures with three different volume fractions (B - D). The force curves have been measured on silicon oxide with a V-shaped silicon nitride cantilever with spring constants around 0.2 N/m. The force has been normalized by dividing by the tip radius.

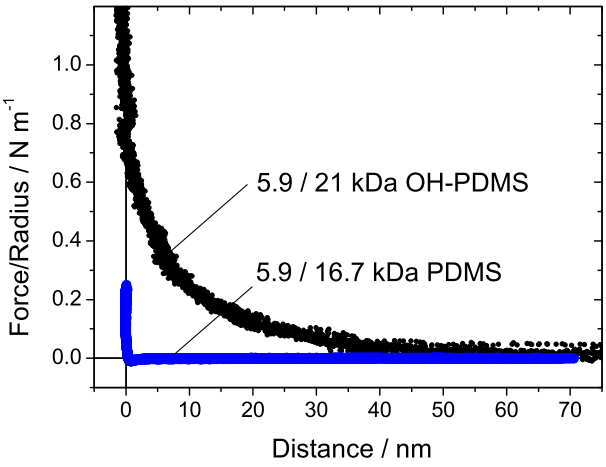

Fig. 4.14: Approaching force curves showing 50:50 (vol%) mixtures of 5.9/16.7 kDa PDMS both methyl terminated and 5.9 kDa methyl-terminated with 21 kDa hydroxyl-terminated PDMS

force was observed (Fig. 4.13 A + B), first in the approach of the force curve ($\varphi_{short} = 0.1$), then also in the retract ($\varphi_{short} = 0.05$). From the curves it is not clear if the change of composition at the interface is linear with the volume fraction, but the measured attraction is a strong indication that the short chains are dominating the surface and preventing the formation of a stable surface layer. This dominance appears only for a negligible enthalpic contribution of the end groups. If the polymer fractions are chemically different, the adsorption to the surface will be dominated by the enthalpic contribution [111, 112]. To verify this forces in melts containing hydroxyl-terminated PDMS (PDMS-OH) were measured. As predicted for PDMS, the terminal hydroxyl groups strongly bind to the oxidized silicon wafer surface and the oxidized silicon nitride tip surface [113]. When mixing hydroxyl-terminated PDMS with low molar mass methyl-terminated PDMS a repulsion is observed for a 50:50 mixture (Fig. 4.14). We interpret the repulsive force as being due to the formation of a brush-like structure of PDMS-OH at the surface. A brush formed by polymer chains with an adsorbing end leads to a steric re-

pulsion [114–120]. To accommodate many hydroxyl groups on the surface the adsorbed chains will deform from the random coil to a more stretched configuration, i.e. a brush-like structure.
The experiments confirm the theoretical predictions of the dominance of short chains at the surface. This behavior is stable for volume fractions down to 10% of short chain PDMS, where a stable surface layer starts forming. The magnitude of the repulsion in PMDS-OH mixtures demonstrates the much stronger interactions for chemically bound polymer layers.

4.3 Superplasticizers

So far, the measurements described have been done in polymer melts and their mixtures. This section focuses on copolymers (superplasticizers) in a CSH equilibrium solution. The sample surface is a CSH crystal, which was precipitated onto a calcite crystal. First, the sample surface was imaged with atomic resolution, to verify the precipitate is indeed CSH. Then the surface interactions between two CSH crystals with and without superplasticizer were measured by taking force curves.

4.3.1 Surface images

CSH surfaces were prepared as described in section 3.3.1 and imaged with the AFM. Two different C/S ratios were used, one with a high $Ca(OH)_2$ fraction of 22 mmol/l, and one with a low fraction of ca. 1 mmol/l. Both CSH surfaces showed spherical but aggregated nanoparticles of ca. 60x30 nm^2 (Fig. 4.15) forming terraces of micrometer size (4.16).
To ensure that the precipitated crystal is CSH, images with atomic resolution have been taken on top of the spherical nanoparticles, where the roughness is small enough. The images reveal, that the resolution is barely good enough to achieve atomic resolution (Fig. 4.17). The resolution decreased by a factor of two inside the glovebox and only one lattice constant is visible in the AFM image, the second can only be extracted from the FFT image with a large error. Reasons for the decrease in resolution are the glovebox, which makes the

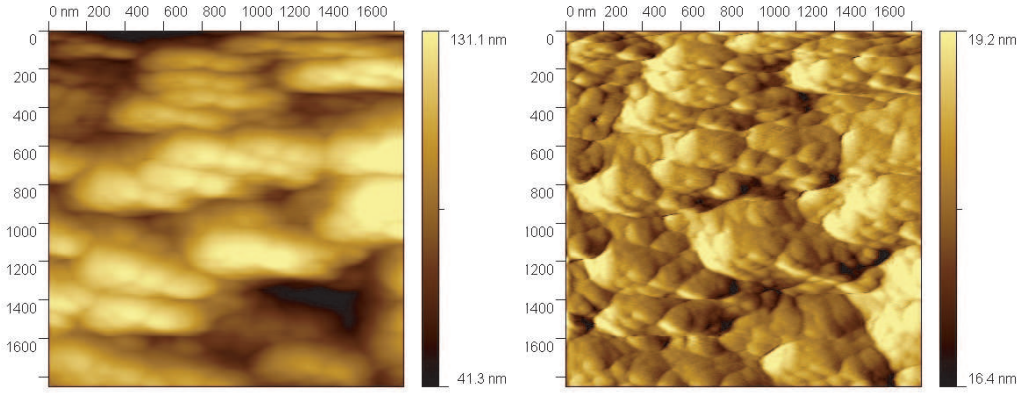

Fig. 4.15: 2x2 µm AFM image of the CSH surface. Left: The height image shows values between 30 and 60 nm for the aggregates which for terraces. Right: The deflection images shows more detailed features and single particles become visible.

system very sensitive to external noise, and the small size of the atomically flat domains. This causes a problem since there is always a small horizontal drift of the sample during the measurement. The atomic resolution images were measured on top of the spherical CSH crystals, and a horizontal drift almost always detaches the tip from the surface, making a new approach necessary.

Nevertheless, although the error is high, the lattice constants could be measured (Tab. 4.3), resulting in a cubic lattice, which is consistent with the CSH surface structure, and which differs clearly from the hexagonal calcite (a = 4.99 Å, b = 8.1 Å) structure. The results ensure, that we obtained a CSH coverage of the calcite.

a / Å	b / Å	α
9,7	5,6	89°
9,9	5,8	105°
9,7	6,5	93°
10,6	4,5	108°

Table 4.3: CSH lattice constants from fourier transformations of AFM images

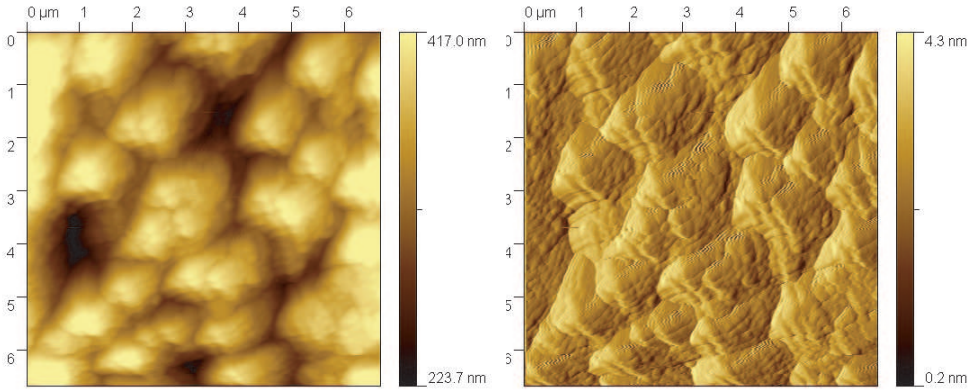

Fig. 4.16: 7x7 µm AFM image of the CSH surface. Left: The height images shows differences of 200 nm between the single terraces, Right: The deflection images shows the more detailed structure, with several flat domains.

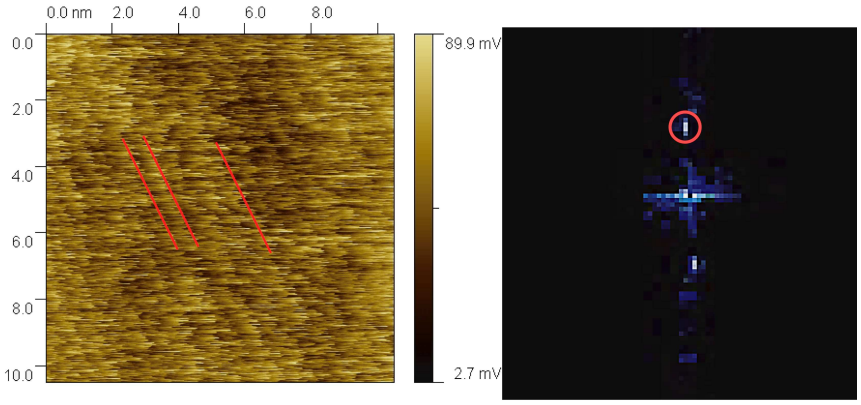

Fig. 4.17: Left: AFM friction image of the CSH lattice with atomic resolution. Right: Fourier transformation of the AFM image. Only one lattice constant can be clearly indentified.

4.3.2 Force-distance curves

The surface interactions between two CSH particles depend on the $Ca(OH)_2$ concentration. For high concentration (22 mmol/l), the interaction is purely attractive, then becomes attracto-repulsive between 1 - 3 mmol/l and purely repulsive for 0.2 mmol/l [98].
The change of surface interaction is due to the change of the concentration of the lime solution, which has three different effects: The increase of the calcium ion concentration, the increase of the pH, and the increase of the ionic strength in solution. According to the DLVO theory, which accounts for the van der Waals forces and the repulsion due to the counterions cloud in solution, an increase in ionic strength in solution condenses the counterion cloud and thus decreases the repulsion. Opposingly, an increase in surface charge density increases the repulsion. Recent studies from Plassard et al. [98] showed, that the DLVO theory is not valid for systems of CSH and lime solution. Increasing the pH while maintaining the ionic strength resulted in a decreasing repulsion.
It was also found that the ionic strength in solution has no influence on the overall interactions. The pH is the most important factor, while the influence of the calcium ion concentration depends on the pH and is discussed in detail in Plassard et al..
Therefore the interactions between a CSH covered tip, and a CSH nanoparticle on the surface should be attractive for highly concentrated lime solutions. The experimental results show indeed the attraction for high concentrations (Fig. 4.18), whether for smaller concentrations, the absence of the attraction led to more unstable interactions and the attracto-repulsive interaction could not be clearly identified.
By introducing superplasticizer into the system, the interaction changed from attractive to repulsive for concentrations of approx. 0.1 vol% of all used superplaticizers. Approach and retract showed a stable, position independent repulsion (Fig. 4.19), which was then fitted with an exponential decay. The decay length increased with increasing side chain length of the superplasticizer (Tab. 4.4).

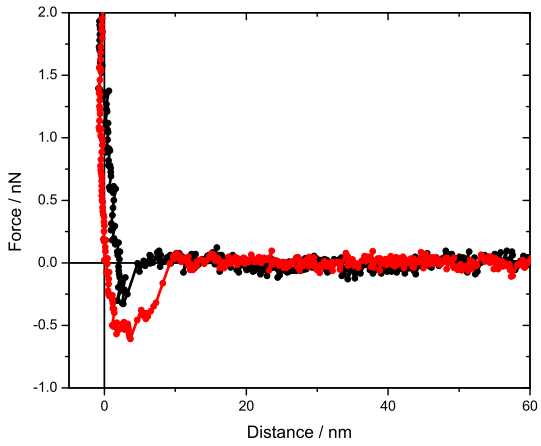

Fig. 4.18: Surface interactions between two CSH particles with high C/S ratio. The calcium ion concentration was 22 mmol/l. Without the superplaticizers, the particles attract each other.(black:approach, red:retract)

Polymer	sidechain length / kDa	λ / nm
SP500	500	0.95
SP3000	3000	2.83
SP6000	6000	3.96

Table 4.4: The decay length increases continuously with the sidechain length.

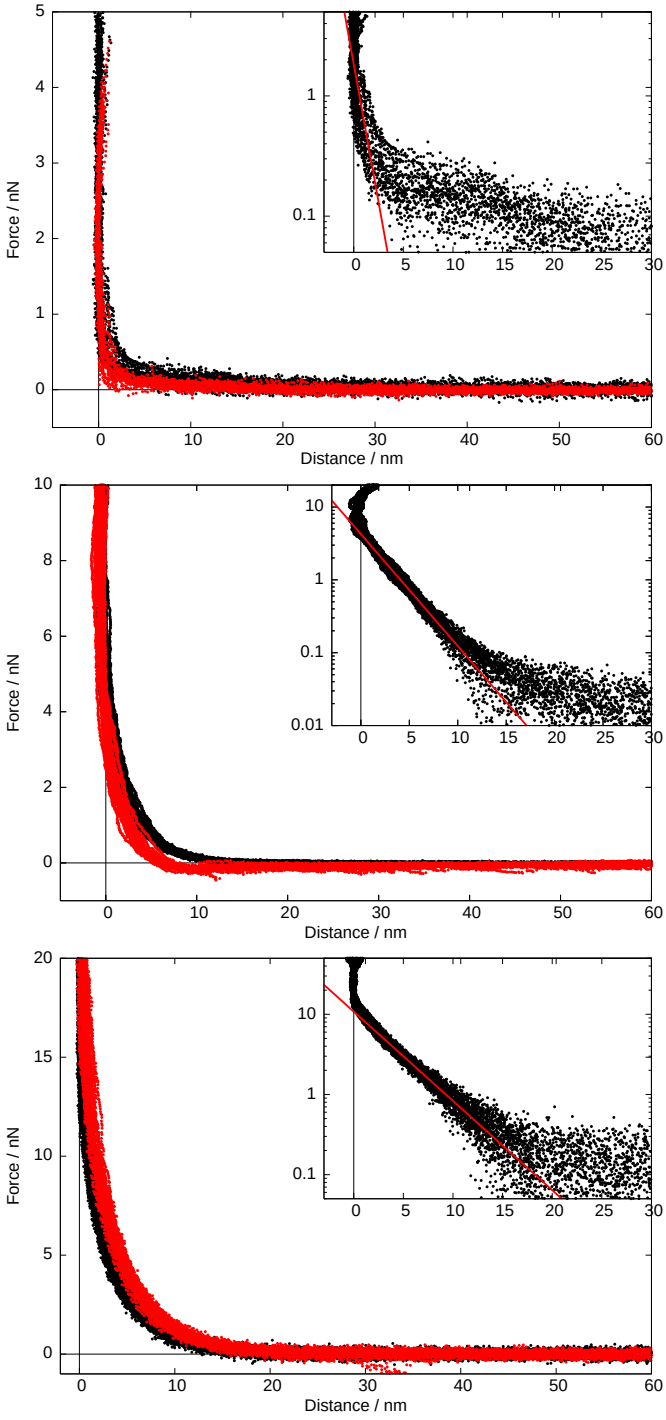

Fig. 4.19: Force curves taken on CSH in presence of superplasticizers with difference sidechain length (black: approach, red: retract). Upper: SP500, λ = 0.95 nm. Middle: SP3000, λ = 2.83 nm. Lower: SP6000, λ = 3.96 nm.

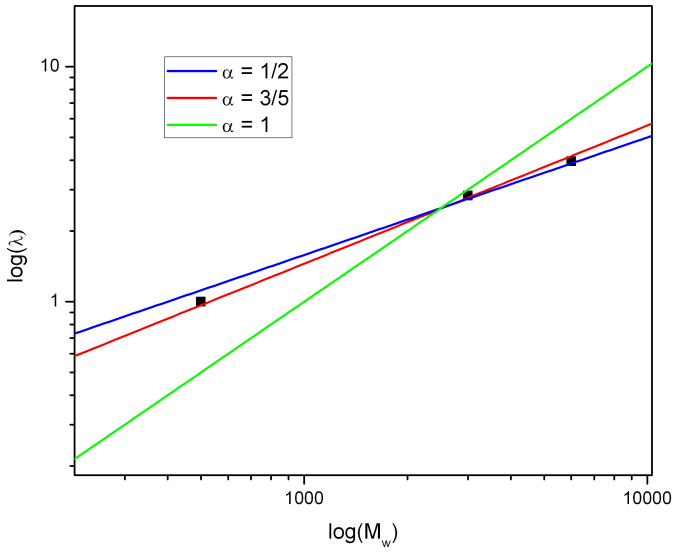

Fig. 4.20: The graph shoes the dependence of the decay length from the molecular weight. Depending of the structure (brush, random coil), the slop changes. Green: brush structure. Blue: ideal random coil, red: random coil with excluded volume)

To decide whether the sidechains of the superplasticizer form a brush on the surface (stretched chains), or if they form random coils ("mushroom regime") the dependence of the decay length of the molecular weight is important. Since the decay length should be proportional the the height of the immobilized surface layer, it should also be proportional to M_w^ν.

$$\lambda \sim M_w^\nu \tag{4.11}$$

If the sidechains have bush-like conformation, ν should be 1, whether for a random coil, the exponent should decrease to 3/5 or 1/2 (See section 2.1.1). By plotting the logarithm of the decay length vs the molecular weight, the increase should be linear with the slope of ν. Figure 4.20 shows the different slopes for ν = 1, 1/2, and 3/5. The best agreement is found for the random coil with excluded volume (ν = 3/5). Although the difference is too small to certainly distinguish different coil formations, the surface layer is obviously not in the brush regime.

In summary, the force curves on CSH surfaces showed the expected change from attractive to repulsive interaction by introducing superplasticizers. The important factor is the sidechain length of the superplasticizer. It was possible to quantify the steric repulsion by fitting with a exponential decay and a decay length λ. The increase of the decay lengths proportional to $M_w^{3/5}$ indicates that the sidechains have a "mushroom" conformation.

5 Conclusion

In this work the existence and/or formation of an adsorbed immobilized polymer layer in PDMS and PI melts in dependence of the molecular weight, and the lattice dimensions and steric interactions of CSH particles with and without addition of superplasticizers was investigated.
For the investigation of the polymer adsorption from a melt, the previous results of layer formation in dependence of the molecular weight for PDMS could be expanded towards hydrodynamic measurements. From the quasi-static measurement, it can be concluded that PDMS forms a stable surface layer for molecular weights above the entanglement molecular weight of 12 kDa. The changing surface interactions at 8 kDa indicates that the time scale for the formation of a stable surface layer is in the order of one minute. This might be longer for longer and entangled PDMS chains. In the hydrodynamic measurements, PDMS showed surface slip for molecular weights below 12 kDa, which is a common property of non-Newtonian fluids. Slip lengths in the order of 5 - 100 nm where measured. For molecular weights above 12 kDa, the slip disappeared which is presumably due to the shift of the shear plane to the top of an adsorbed polymer layer.
In the case of PI, the results under quasi-static conditions showed a weak, short-ranged repulsion, which was slightly stronger for smaller molecular weights. A steric repulsion, and hence a stable surface layer, could not be clearly deduced from the measurements. This results is consistent with predictions from deGennes and Ausseré, and simulations from tenBrinke and Leermakers [2–4, 7]. They agree that no long range force should exist between two surfaces in a polymer melt if a) the polymer is in equilibrium with the bulk reservoir and b) the chains are not pinned at the surface.
Hydrodynamic measurements then confirmed that no surface layer is formed

by PI, since slip was detected in all measurements. As additional indication to the force vs distance curves, velocity vs distance curves were obtained from the measured data, which show an even closer evidence.
Going a step further, by mixing two different chain lengths of chemically identical polymers, theoretical predictions were confirmed, that differences in conformational entropy result in a depletion of the surface layer. Up to this point, investigation of competitive adsorption in melts has been done on deuterated polymer mixtures only. The deuteration modifies the surface interactions to an extent which is comparable to the driving forces of the entropic difference.
It was deduced from the investigation of polymer melts, that adsorbed surface layers influence both, the steric repulsion and the slip boundary condition, thus making it possible to distinguish different adsorbed polymers even in a bimodal mixture. Future work would be to extent the measurements to different surfaces and polymers to gain more evidence on different polymer-surface interactions. Also the interaction between tip, and hydroxy functionalized polymers can be used to investigate bridging events.
For the inverstigation of CSH interactions, the aim was to establish an experimental setup to measure surface forces between two CSH particles. It was possible to precipitate a CSH phase on a calcite crystal that was sufficiently flat to image the lattice dimensions of the CSH, despite the considerable error. Further, it was possible to introduce different superplasticizers into the setup and to measure the surface interactions with and without them. While showing an attractive force for the pure CSH, the addition of the superplasticizers changed the force to a repulsion, which is depending on the molecular weight of the sidechains. The repulsion of the force curve was fitted with an exponential decay and the decay length was found to be proportional to the radius of gyration of the sidechain. Although there is no direct evidence of the layer structure, the assumption can be made that the sidechains are in a coil conformation rather than a stretched brush-like conformation. If a bush-like conformation would apply, the decay length should scale with the number of monomers.
The results of the CSH interactions can be used to compare the interactions

of different industrially used superplasticizers. This does not only include the steric repulsion of the sidechains, but also the effectiveness for different concentrations of the superplasticizer, effects of the ionic strength in solution, and chances for different pH values.

6 Abbreviations

a	monomer length [m], radius of the contact area [m]
A_H	Hamaker constant [J]
b	number of segments per chain
b	slip legnth [m], Kuhn length [m]
C_∞	Flory's ratio
c	polymer concentration [segments / volume]
c_f	concentration of free chains [segments / volume]
d_a, d_b, d_c	lattice constants [m]
d	deflection of the tip [m]
d^*	effective measured deflection [m]
D	distance [m]
E	Young's modulus [Pa]
f	force per area [N m^{-2}]
F	force [N]
h	height [m], thickness [m]
$h\nu$	ionization energies [J]
k_B	Boltzmann constant = $1.380 \cdot 10^{-23} J/K$
k_c	spring constant [N/m]
$k_{distort}$	correction factor
l	bondlength [m]
l_a, l_b	lattice constants [m]
n	refractive index
m	mass [kg]
N	number of monomers per polymer chain
N_K	number of Kuhn monomers
n	number of bonds per chain

$n\varphi$	number of lattice sites occupied by solvent or polymer
Q	electric charge [As]
$r, \vec{r}$	end-to-end distance, vector [m]
r_{max}	contour length [m]
R	radius of a sphere or the cantilever [m]
R_g	radius of gyration [m]
Re	Reynolds number
S_{PSD}	sensitivity of the photodiode [V/nm]
t	time [s]
T	temperature [K]
U_{PSD}	photosensor voltage [V]
v	velocity [m/s]
V	volume [m^3]
w	free energy per surface area [J m^{-2}]
W	free energy [J]
z	distance normal to the surface (z-direction) [m]
z_p	piezo position [m]
α	angle between lattice vectors [°], polarizability [C m^2 V^{-1}]
β^*	correction factor
δ	indentation [m]
ε	dielectric permittivity
η	viscosity [Pa s]
φ	volume fraction
Γ	adsorbed amount [mol m^{-2}]
λ	decay length [m]
μ	dipole moment [C m]
ν	Poisson ratio, frequency [Hz]
ρ	density [kg m^{-3}], molecular densities [molecules per m^3]
ℓ	thickness of the polymer chain [m]
∂	partial derivative

Bibliography

[1] Fleer, G., Cohen Stuart, M., Scheutjens, J., Cosgrove, T., und Vincent, B., *Polymers at Interfaces;* Chapman & Hall, London, 1993.

[2] de Gennes, P., *C.R. Acad. Sci. Paris* **1987**, *305*, 1181–1184.

[3] Ausserré, D. und de Gennes, P., *J. Phys. (Paris)* **1987**, *305*, 1181–1184.

[4] Leermakers, F. und Butt, H.-J., *Phys. Rev. E* **2005**, *72*, 021807.

[5] Müller, M., Albano, E., und Binder, K., *Phys. Rev. E* **2000**, *62*, 5281–5295.

[6] Subbotin, A., Semenov, A., Hadziioannou, G., und ten Brinke, G., *Macromolecules* **1996**, *29*, 1296–1304.

[7] ten Brinke, G., Ausserré, D., und Hadziioannou, G., *J. Chem. Phys.* **1988**, *89*, 4374–4380.

[8] Thompson, P., Grest, G., und Robbins, M., *Phys. Rev. Lett.* **1992**, *68*(23), 3448–3451.

[9] van Alsten, J. und Granick, S., *Macromolecules* **1990**, *23*, 4856–4862.

[10] Horn, R., Hirz, S., Hadziioannou, G., Frank, C., und Catala, J., *J. Chem. Phys.* **1989**, *90*, 6767–6774.

[11] Horn, R. und Israelachvili, J., *Macromolecules* **1988**, *21*, 2836–2841.

[12] Horn, R., Smith, D., und Haller, W., *Chem. Phys. Lett.* **1989**, *162*, 404–408.

[13] Hirz, S., Subbotin, A., Frank, C., und Hadziioannou, G., *Macromolecules* **1996**, *29*, 3970–3974.

[14] Montfort, J. und Hadziioannou, G., *J. Chem. Phys.* **1988**, *88*, 7187–7196.

[15] Ruths, M. und Granick, S., *J. Phys. Chem. B* **1999**, *103*, 8711–8721.

[16] Israelachvili, J., Kott, S., Gee, M., und Witten, T., *Macromolecules* **1989**, *22*, 4247–4253.

[17] Luengo, G., Schmitt, F., Hill, R., und Israelachvili, J., *Macromolecules* **1997**, *30*, 2482–2494.

[18] Georges, J., Millot, S., Loubet, J., und Tonck, A., *J. Chem. Phys.* **1993**, *98*(9), 7345–7360.

[19] Hu, H. und Granick, S., *Science* **1992**, *258*, 1339–1342.

[20] Hu, H., Granick, S., und Schweizer, K., *J. Non-Crystalline Solids* **1994**, *172-174*, 721–728.

[21] Peanasky, J., Cai, L., Granick, S., und Kessel, C., *Langmuir* **1994**, *10*, 3874–3879.

[22] Stark, R., Bonaccurso, E., Kappl, M., und Butt, H. J., *Polymer* **2006**, *47*(20), 7259–7270.

[23] Stark, R., Kappl, M., und Butt, H.-J., *Chinese Polymer J.* **2006**.

[24] Sun, G., Kappl, M., und Butt, H.-J., *Colloids & Surfaces A* **2004**, *250*, 203–209.

[25] Sun, G., Kappl, M., und Butt, H.-J., *European Polymer Journal* **2005**, *41*, 663–667.

[26] Sun, G., Kappl, M., Pakula, T., Kremer, K., und Butt, H.-J., *Langmuir* **2004**, *20*, 8030–8034.

[27] Fetters, L., Lohse, D., Milner, S., und Graessley, W., *Macromolecules* **1999**, *32*, 6847–6851.

[28] Campbell, S., Luengo, G., Srdanov, V., Wudl, F., und Israelachvili, J., *Nature* **1996**, *382*, 520–522.

[29] Homola, A., Nguyen, H., und Hadziioannou, G., *J. Chem. Phys.* **1991**, *94*, 2346–2351.

[30] Yu, C., Evmenenko, G., Kmetko, J., und Dutta, P., *Langmuir* **2003**, *19*, 9558–9561.

[31] de Gennes, P., *Macromolecules* **1982**, *15*, 492–500.

[32] Scheutjens, J. und Fleer, G., *Macromolecules* **1985**, *18*, 1882–1990.

[33] Butt, H.-J., *Biophys. J.* **1991**, *60*, 1438–1444.

[34] Ducker, W., Senden, T., und Pashley, R., *Nature* **1991**, *353*, 239–241.

[35] Hong, P., Boerio, F., und Smith, S., *Macomolecules* **1994**, *27*, 596.

[36] Butt, H.-J., Graf, K., und Kappl, M., *Physics and Chemistry of Interfaces;* Wiley-VCH, Berlin, 2003.

[37] Israelachvili, J., *Intermolecular and Surface Forces;* Academic Press, London, 2 ed., 1992.

[38] Brenner, H., *Chemical engeneering science* **1961**, *16*(3-4), 242–251.

[39] Chan, D. Y. C. und Horn, R. G., *Journal of chemical phusics* **1985**, *83*(10), 5311–5324.

[40] Blake, T., *Colloids & Surfaces* **1990**, *47*, 135–145.

[41] Tolstoi, D., *Dokl. Akad. Nauk CCCP* **1952**, *85*(5), 1089–1092.

[42] Vinogradov, G., Froishteter, G., und Trilisky, K., *Rheol. Acta* **1978**, *17*, 156–165.

[43] Kraynik, A. M. und Schowalter, W. R., *Journal of Rheology* **1981**, *25*(1), 95–114.

[44] Litvinov, V. und Zhdanov, A., *Polymer Science USSR* **1987**, *29*, 1133–1140.

[45] Inn, Y. und Wang, S., *Phys. Rev. Lett.* **1996**, *76*, 467–470.

[46] Migler, K., Hervet, H., und Lger, L., *Phys. Rev. Lett.* **1993**, *70*, 287–290.

[47] Wang, S. und Drda, P., *Macromolecules* **1996**, *29*, 2627–2632.

[48] Mhetar, V. und Archer, L., *Macromolecules* **1998**, *31*, 8607–8616.

[49] Lam, Y. C., Jiang, L., Yue, C. Y., Tam, K. C., und Li, L., *Journal of Rheology* **2003**, *47*(3), 795–807.

[50] Yang, X., Ishida, H., und Wang, S., *J. Rheology* **1998**, *42*, 63–80.

[51] Horn, R., Vinogradova, O., Mackay, M., und Phan-Thien, N., *J. Chem. Phys.* **2000**, *112*, 6424–6433.

[52] Brochard, F. und de Gennes, P., *Langmuir* **1992**, *8*, 3033–3037.

[53] Hatzkiriakos, S. und Kalogerakis, N., *Rheol. Acta* **1994**, *33*, 38–47.

[54] Hill, D., *J. Rheol.* **1998**, *42*, 581–601.

[55] Joshi, Y., Lele, A., und Mashelkar, R., *J. Non-Newtonian Fluid Mech.* **2000**, *94*, 135–149.

[56] Yarin, X. und Graham, M., *J. Rheol.* **1998**, *42*, 1419–1504.

[57] Ajdari, A., Brochard-Wyart, F., Gay, C., de Gennes, P., Viovy, L., Barrat, J., und Bocquet, L., *J. Phys. (France)* **1999**, *82*, 4671–4674.

[58] Barrat, J. und Bocquet, L., *Phys. Rev. Lett.* **1999**, *82*, 4671–4674.

[59] Gupta, S., Cochran, H., und Cummings, P., *J. Chem. Phys.* **1997**, *107*, 10316–10326.

[60] Thompson, P. und Troian, S., *Nature* **1997**, *389*, 360–362.

[61] Sun, M. und Ebner, C., *Phys. Rev. Lett.* **1992**, *69*, 3491–3494.

[62] Bonaccurso, E., Kappl, M., und Butt, H.-J., *Phys. Rev. Lett.* **2002**, *88*(7), 076103.

[63] Bonaccurso, E., Butt, H.-J., und Craig, V., *Phys. Rev. Lett.* **2003**, *90*, 144501.

[64] Craig, V., Neto, C., und Williams, D., *Phys. Rev. Lett.* **2001**, *87*, 4504–4507.

[65] Denn, M., *Annu. Rev. Fluid Mech.* **1990**, *22*, 13–34.

[66] Esperidião, M., *Ind. Eng. Chem. Res.* **2003**, *42*, 5819–5826.

[67] Hartmann, L., Kremer, F., Pouret, P., und Léger, L., *J. Chem. Phys.* **2003**, *118*, 6052–6058.

[68] Léger, L., *J. Phys.: Condens. Matter* **2003**, *15*, S19–S29.

[69] Léger, L., Hervet, H., Marciano, Y., Deruelle, M., und Massey, G., *Israel Journal of Chemistry* **1995**, *35*(1), 65–74.

[70] Pit, R., Hervet, H., und Léger, L., *Phys. Rev. Lett.* **2000**, *85*, 980–983.

[71] Sun, G., Bonaccurso, E., Franz, V., und Butt, H.-J., *J. Chem. Phys.* **2002**, *117*, 10311–10314.

[72] Vinogradova, O. I., *Langmuir* **1995**, *11*(6), 2213–2220.

[73] Zhu, Y. und Granick, S., *Phys. Rev. Lett.* **2001**, *87*(9), 096105.

[74] Zhu, Y. und Granick, S., *Macromolecules* **2002**, *35*, 4658.

[75] Vinogradova, O., *Int. J. Miner. Process.* **1999**, *56*, 31–60.

[76] Vinogradova, O., Bunkin, N., Churaev, N., Kiseleva, O., Lobeyev, A., und Ninham, B., *J. Colloid Interface Sci.* **1995**, *173*, 443–447.

[77] Granick, S., Kumar, S. K., Amis, E. J., Antonietti, M., Balazs, A. C., Chakraborty, A. K., Grest, G. S., Hawker, C., Janmey, P., Kramer, E. J., Nuzzo, R., Russell, T. P., und Safinya, C. R., *Journal of Polymer Science Part B-Polymer Physics* **2003**, *41*(22), 2755–2793.

[78] Léger, L., Hervet, H., Massey, G., und Durliat, E., *Journal of Physics-Condensed Matter* **1997**, *9*(37), 7719–7740.

[79] Hertz, H. und Johnson, K., *Contact Mechanics;* Vol. 92; Cambridge University Press, Cambridge, 1985.

[80] Johnson, K., *Contact Mechanics;* Cambridge University Press, Cambridge, 1985.

[81] Binnig, G., Quate, C. F., und Gerber, C., *Phys. Rev. Lett.* **1986**, *56*, 930–933.

[82] Butt, H.-J., Cappella, B., und Kappl, M., *Surf. Sci. Rep.* **2005**, *59*, 1–152.

[83] Sader, J., Chou, J., und Mulvaney, P., *Rev. Sci. Instrum.* **1999**, *70*(10), 3967–3969.

[84] Torii, A., Sasaki, M., Hane, K., und Shigeru, O., *Meas. Sci. Technol.* **1996**, *7*, 179–184.

[85] Burnham, N. A., Chen, X., Hodges, C., Matei, G., Thoreson, E., Roberts, C., Davies, M., und Tendler, S., *Nanotechnology* **2003**, *14*, 1–6.

[86] Butt, H.-J. und Jaschke, M., *Nanotechnology* **1995**, *6*, 1–7.

[87] Hutter, J. und Bechhoefer, J., *Rev. Sci. Instrum.* **1993**, *64*, 1868–1873.

[88] Mitchell, L. D., Prica, M., und Birchall, J. D., *Journal of materials science* **1996**, *31*(16), 4207–4212.

[89] Garrault, S., Behr, T., und Nonat, A., *Journal of physical chemistry B* **2006**, *110*(1), 270–275.

[90] Nachbaur, L., Mutin, J. C., Nonat, A., und Choplin, L., *Cement and Concrete Research* **2001**, *31*(2), 183–192.

[91] Jönsson, B., Nonat, A., Labbetz, C., Cabane, B., und Wennerström, H., *Langmuir* **2005**, *21*, 9211– 9221.

[92] Nonat, A., *Cement and concrete research* **2004**, *34*(9), 1521–1528.

[93] Plassard, C., Lesniewska, E., Pochard, I., und Nonat, A., *Ultramicroscopy* **2004**, *100*(3-4), 331–338.

[94] Uchikawa, H., Hanehara, S., und Sawaki, D., *Cement and Concrete Research* **1997**, *27*(1), 37–50.

[95] Lesko, S., Lesniewska, E., Nonat, A., Mutin, J. C., und Goudonnet, J. P., *Ultramicroscopy* **2001**, *86*(1-2), 11–21.

[96] Yang, T. H., Keller, B., und Magyari, E., *Journal of physics D - applied physics* **2002**, *35*(8), L25–L28.

[97] Gauffinet, S., Finot, E., Lesniewska, R., und Nonat, A., *Comptes rendus de l academie des sciences serie II fascicule a-sciences de la terre et des planetes* **1998**, *327*(4), 231–236.

[98] Plassard, C., Lesniewska, E., Pochard, I., und Nonat, A., *Langmuir* **2005**, *21*(16), 7263–7270.

[99] Kauppi, A., Andersson, K. A., und Bergstrom, L., *Cement and Concrete Research* **2005**, *35*(1), 133–140.

[100] Preuss, M. und Butt, H.-J., *Langmuir* **1998**, *14*, 3164–3174.

[101] Raiteri, R., Preuss, M., Grattarola, M., und Butt, H.-J., *Colloids and Surfaces A* **1998**, *136*, 191–197.

[102] Bonaccurso, E.; *Investigation of electrokinetic forces on single particles;* Dissertation, Universitt-Gesamthochschule-Siegen, **2001**.

[103] Snétivy, D. und Vancso, G. J., *Langmuir* **1993**, *9*(9), 2253–2254.

[104] Jaschke, M., Schönherr, H., Wolf, H., Butt, H.-J., Bamberg, E., Besocke, M., und Ringsdorf, H., *J. Phys. Chem.* **1996**, *100*, 2290–2301.

[105] Litvinov, V., Barthel, H., und Weis, J., *Macromolecules* **2002**, *35*, 4356–4364.

[106] Mertsch, R. und Wolf, B., *Macromolecules* **1994**, *27*, 3289–3294.

[107] Siedle, P., Butt, H.-J., Bamberg, E., Wang, D., Kühlbrandt, W., Zach, J., und Haider, M., *Inst. Phys. Conf. Ser.* **1992**, *130*, 361–364.

[108] Vesenka, J., Miller, R., und Henderson, E., *Rev. Sci. Instrum.* **1994**, *65*(7), 2249–2251.

[109] Neto, C. und Craig, V., *Langmuir* **2001**, *17*, 2097–2099.

[110] Vinogradova, O. und Yakubov, G., *Langmuir* **2003**, *19*, 1227–1234.

[111] Jalbert, C., Koberstein, J., Hariharan, A., und Kumar, S., *Macomolecules* **1997**, *30*, 4481.

[112] Manghi, M. und Aubouy, M., *Adv. Colloid Interface Sci* **2001**, *94*, 21–31.

[113] Tsige, M., Soddemann, T., Rempe, S., Grest, G., Kress, J., Robbins, M., Sides, S., Stevens, M., und Webb, E., *J. Chem. Phys.* **2003**, *118*, 5132–5142.

[114] Ash, S. und Findenegg, G., *Trans. Faraday Soc.* **1971**, *67*, 2122.

[115] Dolan, A. und Edwards, S., *Proc. R. Soc. London A* **1974**, *337*, 509–516.

[116] de Gennes, P., *Adv. Colloid Interface Sci.* **1987**, *27*, 189–209.

[117] Klein, J., Perahia, D., und Warburg, S., *Nature* **1991**, *352*, 143–145.

[118] Milner, S., Witten, T., und Cates, M., *Macromolecules* **1988**, *21*, 2610–2619.

[119] Patel, S., Tirrell, M., und Hadziioannou, G., *Colloids & Surf.* **1988**, *31*, 157–179.

[120] Taunton, H., Toprakcioglu, C., Fetters, L., und Klein, J., *Macromolecules* **1990**, *23*, 571–580.